Title

Mitochondria Bound to Lipid Droplets Have Unique Bioenergetics, Composition, and Dynamics that Support Lipid Droplet Expansion

Journal

Cell Metabolism, 27(4)

ISSN

1550-4131

Authors

Benador, Ilan Y
Veliova, Michaela
Mahdaviani, Kiana
et al.

Publication Date

2018-04-01

DOI

10.1016/j.cmet.2018.03.003

Peer reviewed

HHS Public Access

Author manuscript

Cell Metab. Author manuscript; available in PMC 2019 April 03.

Published in final edited form as:

Cell Metab. 2018 April 03; 27(4): 869–885.e6. doi:10.1016/j.cmet.2018.03.003.

Mitochondria Bound to Lipid Droplets Have Unique Bioenergetics, Composition, and Dynamics That Support Lipid Droplet Expansion

Ilan Y. Benador[1,2], **Michaela Veliova**[1,10], **Kiana Mahdaviani**[2,10], **Anton Petcherski**[1], **Jakob D. Wikstrom**[3,4], **Essam Assali**[1,5], **Rebeca Acín-Peréz**[1], **Michael Shum**[1], **Marcus F. Oliveira**[6], **Saverio Cinti**[7], **Carole Sztalryd**[8], **William D. Barshop**[9], **James A. Wohlschlegel**[9], **Barbara E. Corkey**[2], **Marc Liesa**[1,*], and **Orian S. Shirihai**[1,2,5,11,*]

[1]Division of Endocrinology, Department of Medicine, and Department of Molecular and Medical Pharmacology, David Geffen School of Medicine at UCLA, Los Angeles, CA, USA.

[2]Obesity Research Center, Department of Medicine, Boston University School of Medicine, Boston, MA, USA.

[3]Dermatology and Venereology Unit, Department of Medicine, Karolinska Institutet, Stockholm, Sweden.

[4]Department of Dermato-Venereology, Karolinska University Hospital, Stockholm, Sweden.

[5]Department of Clinical Biochemistry, School of Medicine, Ben Gurion University of The Negev, Beer-Sheva, Israel.

[6]Institute of Medical Biochemistry Leopoldo de Meis, Universidade Federal do Rio de Janeiro, Rio de Janeiro, Brazil.

[7]Department of Experimental and Clinical Medicine, University of Ancona, Ancona, Italy.

[8]Department of Medicine, School of Medicine, University of Maryland Baltimore, MD 21201 USA.

[9]Department of Biological Chemistry, University of California, Los Angeles, CA, USA.

[*]Correspondence: mliesa@mednet.ucla.edu (M.L.), oshirihai@mednet.ucla.edu (O.S.S.).

[10]These authors contributed equally

[11]Lead Contact

SUPPLEMENTAL INFORMATION

Supplemental Information includes five figures and can be found with this article online at …

AUTHOR CONTRIBUTIONS

IYB wrote the manuscript, performed experiments and image analysis, and designed the study. OSS and ML helped design the study and supervised manuscript writing. KM performed respirometry and NADH experiments and helped design the study. MV and AP performed Plin5 imaging and respirometry experiments. EA performed citrate synthase experiments. RAP performed cytochrome c oxidase experiments and helped optimize blue native PAGE and ATP synthase experiments. JDW performed PAGFP and Drp1 image acquisition. SC performed electron microscopy processing and image acquisition. WDB and JAW performed mass spectrometry proteomics. BEC, MS, MFO, CS, and ML helped with experiments and data interpretation. All authors read and approved the final version of the manuscript.

CONFLICTS OF INTEREST

The authors declare that they have no conflict of interest.

Summary

Mitochondria associate with lipid droplets (LDs) in fat-oxidizing tissues but the functional role of these peridroplet mitochondria (PDM) is unknown. Microscopic observation of interscapular brown adipose tissue reveals that PDM have unique protein composition and cristae structure, and remain adherent to the LD in the tissue homogenate. We developed an approach to isolate PDM based on their adherence to LDs. Comparison of purified PDM to cytoplasmic mitochondria reveals that (1) PDM have increased pyruvate oxidation, electron transport, and ATP synthesis capacities. (2) PDM have reduced beta oxidation capacity and depart from LDs upon tissue activation of thermogenesis and beta oxidation. (3) PDM support LD expansion as Perilipin 5-induced recruitment of mitochondria to LDs increases ATP-dependent triglyceride synthesis. (4) PDM maintain a distinct protein composition due to uniquely low fusion-fission dynamics. We conclude that PDM represent a segregated mitochondrial population with unique structure and function that supports triglyceride synthesis.

eTOC Blurb

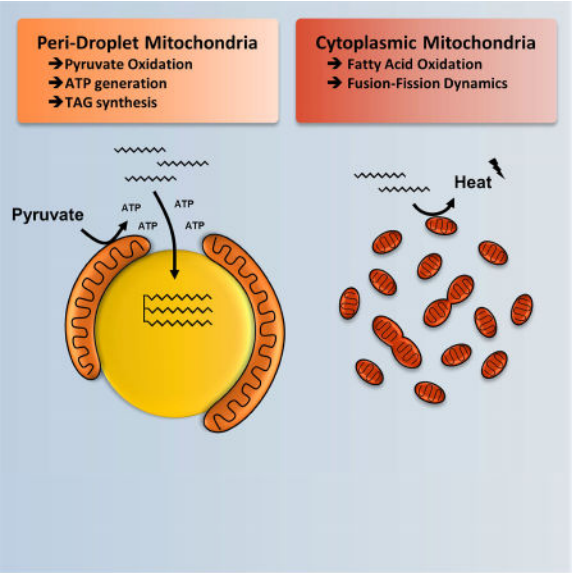

The functional role of lipid droplet-associated mitochondria is currently unknown. Benador et al. demonstrate that peri-droplet mitochondria (PDM) have enhanced bioenergetic capacity and reduced fatty acid oxidation capacity. PDM promote lipid droplet expansion by providing ATP for triglyceride synthesis. PDM maintain distinct metabolic identity by having reduced fusion-fission dynamics.

Keywords

Mitochondria; lipid droplet; brown adipose tissue; peridroplet mitochondria; mitochondrial dynamics

INTRODUCTION

Studies have shown that mitochondria contact lipid droplets (LDs) in tissues with high fatty acid storage and oxidation capacity, including brown adipose tissue (Boutant et al., 2017), heart (Wang et al., 2013), and Type I skeletal muscle (Tarnopolsky et al., 2007). Furthermore, mitochondria-LD association was shown to be highly regulated by Perilipin5 (Plin5), a LD coat protein highly expressed in fat-oxidizing tissues (Wang et al., 2011). The high degree of regulation and tissue-specificity support the concept that peridroplet mitochondria (PDM) play a specialized role in fat metabolism. However, it remains unclear whether PDM promote lipid oxidation (Rambold et al., 2015), lipid storage (Nguyen et al., 2017; Stone et al., 2009; Wang et al., 2011), or both.

In this study, we sought to determine the role of PDM in a system where a robust shift can occur between fat storage and oxidation. Brown adipose tissue (BAT) acutely turns on uncoupled lipid oxidation upon adrenergic stimulation (Cannon and Nedergaard, 2004). Functional specialization and segregation of mitochondrial subpopulations may allow BAT mitochondria to perform the contradictory tasks of uncoupled fatty acid oxidation and ATP generation for fatty acid activation by Coenzyme A (CoA) addition. However, it remains unclear whether functional specialization and segregation is possible in brown adipocytes where fusion and fission continuously equilibrate the content across the mitochondrial population within each adipocyte (Wikstrom et al., 2014). Furthermore, there are currently no established methods to isolate PDM, leaving their function, composition, and bioenergetics unknown.

In this study, we developed an approach to isolate PDM from BAT based on their adherence to LDs. Our results demonstrate that PDM represent a segregated mitochondrial subpopulation with distinct composition, bioenergetics, and dynamics that support triglyceride synthesis.

RESULTS

Isolation of peridroplet mitochondria by differential centrifugation

Little is currently known about peridroplet mitochondria (PDM) due to the lack of reliable methods to selectively isolate PDM. The tight association between mitochondria and lipid droplets (LDs) observed in electron micrographs (EMs)(Wikstrom et al., 2014) and in biochemical studies (Yu et al., 2015) led us to hypothesize that mitochondria-LD association could withstand mechanical cell disruption. To test this, we disrupted interscapular brown adipose tissue (BAT) using a dounce homogenizer, separated the fat layer by low-speed centrifugation, and co-stained it with the neutral lipid dye BODIPY 493/503 (BODIPY) and the mitochondrial dye MitoTracker deep red (MitoTracker)(Figure 1A). Super-resolution confocal microscopy revealed numerous LDs surrounded by tubular MitoTracker-stained structures, suggesting that mitochondria-LD association was preserved in the fat layer (Figure 1B). Next, to separate PDM from LDs, we centrifuged the fat layer at high speed, a procedure previously shown to strip LD proteins (Ding et al., 2013). The stripped fat layer contained over 50% fewer LDs with MitoTracker fluorescence (Figures 1C–D), suggesting that LDs were effectively stripped of PDM. The resulting peridroplet mitochondrial (PDM)

pellet contained MitoTracker-positive particles and little to no BODIPY staining (Figure 1E), suggesting that PDM were successfully separated from LDs. To confirm that PDM were not contaminated with LD remnants, we quantified the LD content under low magnification microscopy (Figure 1F–G). Low-magnification images revealed that PDM pellet had over 95% lower LD content compared to the fat layer (Figure 1G). Furthermore, the level of LD contamination within the PDM pellet was similar to the LD contamination within the cytoplasmic mitochondria (CM) pellet isolated from the supernatant (Figures 1A, 1G). These results suggest that LDs were effectively removed from PDM by differential centrifugation.

Since differential centrifugation results in relatively crude preparations, we next determined the mitochondrial protein content in CM and PDM fractions by mass spectrometry. Protein annotation using MitoCarta2.0 (Calvo et al., 2016) revealed that 5969 out of 10935 (54.5%) identified peptides belonged to mitochondrial proteins in PDM compared to 5979 out of 11812 (50.6%) in CM (Figure 1H). Furthermore, analysis of previously published BAT mitochondria proteomics data revealed a 46.9% enrichment of mitochondrial protein (Table S4) (Forner et al., 2009). These results suggest that mitochondrial protein enrichment in CM and PDM fractions were comparable and within the range of previously published methods.

Next, to determine whether CM and PDM preparations can generate a similar membrane potential, we stained the preparations with the membrane potential-sensitive rosamine dye MitoTracker Red. To control for mitochondrial mass, we co-stained preparations with the mitochondrial protein dye MitoTracker Green (Cottet-Rousselle et al., 2011). Fluorescence microscopy revealed no significant differences in the MitoTracker Red-to-Green fluorescence ratio between CM and PDM (Figures 1I–J), suggesting that CM and PDM preparations were equally capable of generating a membrane potential.

Peridroplet mitochondria have increased respiratory capacity

To characterize the respiratory capacity of PDM, we measured their oxygen consumption rate using Seahorse XF96 extracellular flux analyzer. Isolated PDM and CM were loaded into different wells of the same seahorse plate and assayed with pyruvate and malate as fuels. Prior to the assay, we confirmed that equal levels of mitochondrial protein and functional mitochondria were present in CM and PDM preparations by mass spectrometry analysis (Figure 1H) and membrane potential imaging (Figures 1I–J), respectively. Furthermore, we confirmed equal mitochondrial mass was loaded into the XF96 flux analyzer plate by directly staining and imaging the wells with MitoTracker (Figures 2A–B).

PDM assayed using pyruvate and malate as fuels showed a 2-fold increase in both ATP-synthesizing respiration (State III) and maximal respiratory capacity induced by uncoupling with FCCP (Maximal) when compared to CM (Figures 2C–E). Enhanced ATP synthesis and maximal electron transport capacities in PDM were not limited to pyruvate oxidation since a similar increase was observed when assayed with the fuel succinate (Figure S1).

To determine whether increased PDM respiratory capacity is associated with higher capacity of respiratory enzyme complexes, we next assessed the activity of individual complexes in isolated mitochondria. Cytochrome c oxidase (COX) activity was determined by measuring

oxygen consumption rate using TMPD/ascorbate. We injected Antimycin and rotenone at the start of the assay and the COX-specific inhibitor sodium azide at the end of the assay to confirm that TMPD/ascorbate-driven respiration was specific to COX activity. TMPD/ascorbate-driven respiration was 68±27.5% higher in PDM compared to CM (Figures 2F–G), confirming that isolated PDM have higher COX activity compared to CM.

Next, we determined ATP synthase function in isolated mitochondria using firefly luciferase luminescence. We determined the optimal concentration of reagents and photometric measurement settings using HPLC-purified ATP standards and controlled for non-mitochondrial ATP synthesis using the ATP synthase inhibitor oligomycin. PDM had 210.4±62.8% higher rate of luminescence increase compared to CM (Figures 2H–I), confirming isolated PDM have higher ATP synthesis capacity compared to CM.

Next, to determine whether higher respiratory capacity observed in isolated PDM can be detected in living cells, we assessed mitochondrial membrane potential using the reversible membrane potential-sensitive dye tetramethylrhodamine-ethyl-ester-perchlorate (TMRE). TMRE fluorescence intensity was not significantly different between CM and PDM at baseline, suggesting that increased PDM proton pumping by electron transport complexes may be matched by higher proton flux through ATP synthase. If this were the case, we reasoned that blocking ATP synthase will cause an acute hyperpolarization of PDM as compared to CM. Indeed, oligomycin treatment revealed PDM with higher TMRE fluorescence intensity compared to CM (Figures 2J–K), suggesting that PDM have higher proton efflux rate compared to CM. Taken together, these results suggest that PDM have enhanced oxidative phosphorylation capacity.

Peridroplet mitochondria have increased levels of cytochrome c oxidase, ATP synthase, and super complex I+III assembly

We reasoned that increased electron transport and ATP synthesis capacities in PDM could result from increased expression levels of protein associated with oxidative phosphorylation. To test this, we assessed levels of each OXPHOS complex by Western blot analysis of complex subunits. We confirmed equal amounts of protein were loaded by staining Western blot membranes with the non-specific protein dye Ponceau S (Figure 3A). To control for mitochondrial protein loading, bands were normalized to the mitochondrial marker Tom20, which did not vary significantly between samples (Figure S2A–B).

Western blot analysis revealed that PDM have 15.6±4.5% higher levels of cytochrome c oxidase subunit 4 (COX4) protein and 8.7±4.8% higher ATP Synthase subunit α (ATP Synthase) protein relative to CM (Figures 3B–C). We confirmed that detected differences were independent of loading and band saturation by performing a dilution blot and histogram analysis, respectively (Figures S2C–F). We observed no significant differences in Complex I, Complex II, nor Complex III subunit levels (Figures 2B–C). Given the relatively small differences in complex protein levels, we rationalized that enhanced PDM respiratory capacity could be due to increased assembly of respiratory super complexes (Lapuente-Brun et al., 2013; Rosca et al., 2008). To test this, we measured super-complex assembly by blue native PAGE. Remarkably, Blue native PAGE revealed 29.5±8.2% higher levels of Complex I + Complex III super-assembly in PDM relative to CM (Figures 3D–E). These results

suggest that specialized OXPHOS protein composition and super assembly may contribute to enhanced PDM respiratory capacity.

High levels of cytochrome c oxidase and ATP synthase are preferentially localized to PDM

To determine the relative levels of OXPHOS proteins in CM and PDM within intact brown adipocytes we next measured protein levels by immunofluorescence. We confirmed antibody specificity by probing a whole Western blot membrane with each individual antibody and exclusively detecting a single band corresponding to the protein of interest (Figure S2G). Super-resolution confocal imaging of immunostained cells revealed heterogeneous distribution of OXPHOS protein in PDM and CM populations (Figures 3F–I). Subcellular distribution analysis revealed that mitochondria with the highest levels of COX4 and ATP synthase α are exclusively PDM. Remarkably, some LDs were surrounded by ATP synthase-rich PDM, while other LDs within the same cell were surrounded by PDMs with lower ATP synthase levels comparable to CM. This remarkable heterogeneity may explain the relatively small changes we detected by Western blot analysis of the average protein expression of isolated CM and PDM.

Peridroplet mitochondria have lower fatty acid oxidation capacity but increased TCA cycle capacity

Our results show that PDM have enhanced OXPHOS protein levels and respiratory capacity. However, these results were not sufficient to determine whether PDM have a preference for fuel oxidation by beta oxidation or through the TCA cycle. If PDM are specialized for fat oxidation, we reasoned that 1. isolated PDM will have enhanced fatty acid oxidation capacity, 2. PDM will have enhanced levels of uncoupling protein 1 (UCP1), and 3. mitochondrial contact with LDs will be increased during cold-induced thermogenesis, when fatty acid oxidation rate is maximal.

To test these predictions, we measured fatty acid-driven respiration and UCP1 content in isolated mitochondria. Contrary to our prediction, maximal respiration driven by palmitoyl-carnitine was significantly lower in PDM compared to CM (Figures 4A–B). We confirmed that PDM have reduced fatty acid oxidation capacity by normalizing fat oxidation capacity to pyruvate oxidation capacity assayed in parallel wells on the same seahorse XF96 plate (Figure S3). Furthermore, Western blot analysis showed no difference in UCP1 levels (Figure 4C), suggesting that PDM are not specialized for thermogenic fat oxidation.

Since mitochondrial beta oxidation and TCA flux are two competing pathways (Garland et al., 1968), we next tested whether enhanced PDM respiratory capacity is supported by higher capacity for TCA cycling. To this end, we determined the activity of the TCA enzyme citrate synthase (CS) by 5,5′-dithio-bis(2-nitrobenzoic acid) (DTNB) absorbance assay. DTNB reduction rate was 33.1±9.7% higher in isolated PDM compared to CM (Figures 4D–E), suggesting higher TCA cycle capacity. We next measured NAD(P)H levels in cultured primary brown adipocytes using live cell fluorescence microscopy. NAD(P)H levels as measured by 450nm emission were 30.8±3.5% higher in PDM compared to CM (Figures 4F–G), consistent with CS measurements (Figures 4D–E). Taken together, these results

suggest that enhanced ATP synthesis and electron transport capacity in PDM are supported by increased substrate oxidation through the TCA cycle.

Mitochondria-LD contact is decreased upon activation of thermogenic fatty acid oxidation *in vivo*

The reduced fatty acid oxidation capacity observed in isolated PDM suggested that PDM are not specialized for fat oxidation. To determine the relation between PDM and fatty acid oxidation *in vivo*, we next assessed mitochondria-LD contact in BAT harvested from cold-adapted animals, where fatty acid oxidation is maximized to produce heat. If PDM play a significant role in fatty acid oxidation, we predicted that mitochondria-LD contact will be increased in cold-exposed mice compared to mice adapted to thermoneutral conditions, where fatty acids are stored in LDs. Contrary to our predictions, the number of mitochondria in contact with LDs was over 50% lower in cold-exposed mice compared to thermoneutral conditions (Figures 4H–I). Quantitative image analysis confirmed this: Mitochondria-LD contact area represented only 3.8±1.0% of mitochondrial perimeter in cold-exposed mice compared to 24.7±3.7% in thermoneutral conditions (Figure 4J). To control for reduced LD surface area resulting from lipid oxidation during cold exposure, we quantified mitochondria-LD contact area as a proportion of LD perimeter (Figure 4K). Mitochondria-LD contact as a proportion of LD surface was reduced by over 75% in cold exposed animals, confirming that mitochondria-LD contact is reduced by cold exposure. These results suggest that mitochondria-LD contact is negatively associated with fatty acid oxidation *in vivo*.

Mitochondria-lipid droplet association promotes lipid droplet expansion

The high level of mitochondria-LD contact observed in thermoneutral conditions led us to hypothesize that mitochondria-LD contact plays a role in LD expansion rather than oxidation. To test this, we sought to create an experimental system where mitochondrial association to LDs can be induced. Plin5 is a LD-coating protein that is uniquely capable of recruiting mitochondria to LDs (Bosma et al., 2012; Wang et al., 2013) through its C-terminal region (Figure 5A) (Wang et al., 2011). We therefore assessed the effect of adenovirus-mediated Plin5 overexpression on LD expansion in cultured brown adipocytes.

To determine mitochondrial association to LDs we stained transduced cells with TMRE to label the mitochondrial network and BODIPY 493/503 (BODIPY) to label LDs. Confocal microscopy revealed that cells expressing the full version of Plin5 that includes its mitochondrial recruiting sequence (Plin5) significantly increased mitochondrial recruitment to LDs relative to untransduced control cells (Figures 5B–C). We confirmed the mitochondrial recruitment phenotype was not due to increased LD content as large areas of the cytosol remained free of LDs and mitochondria in cells over expressing Plin5 (Figure S4A, Figures 5G).

To control for Plin5 effects that are not related to mitochondrial recruitment, we overexpressed a truncated version of Plin5 that lacks the C-terminal mitochondrial recruiting sequence (Plin5Δ399-463). Confocal imaging confirmed that Plin5Δ399-463 did not significantly increase mitochondrial recruitment to LDs relative to untransduced control cells (Figures 5B–C). Next, to determine the effect of Plin5-mediated mitochondrial

recruitment to LDs on bioenergetic capacity, we performed respirometry on intact transduced cells. Cells expressing the full version of Plin5 that contains the mitochondrial recruiting sequence had 83.2±24.0% higher ATP-linked respiration and 54.1±28.6% higher spare respiratory capacity compared to cells expressing truncated Plin5Δ399-463 that lacks the mitochondrial recruiting sequence (Figure S4B–E). These results confirmed that mitochondrial recruitment to LDs by Plin5 promotes increased respiratory capacity, in agreement with data from isolated PDM (Figures 2A–C).

Next, to determine the effect of mitochondrial recruitment on lipid accumulation, we quantified LD area in confocal microscopy images. Quantitative image analysis revealed that cells expressing the full version of Plin5 that contains mitochondrial recruiting sequence (Plin5) had significantly higher LD accumulation (Figure 4D) and size (Figure 5E) compared to cells expressing the truncated version of Plin5 that lacks the mitochondrial recruiting sequence (Plin5Δ399-463). We confirmed these effects were not related to lipolysis regulation as overexpression of Plin5 and Plin5Δ399-463 reduced lipolysis to the same extent (Figure 5F). These results suggest that mitochondrial association to LDs promotes LD expansion independent of lipolysis regulation.

To determine whether this phenomenon is unique to brown adipocytes, we repeated this experimental series in INS1, a pancreatic beta cell line with low levels of endogenous perilipin expression and lipogenic capacity (Figure 5G). Consistent with brown adipocytes, over 80% of mitochondria were recruited to LDs in INS1 cells expressing Plin5 compared to less than 12% in Plin5Δ399-463 (Figure 5H). Furthermore, LD accumulation and size were significantly higher in INS1 cells expressing Plin5 compared to Plin5Δ399-463 (Figures 5I–J). These results suggest that mitochondrial contact with LDs promotes the expansion of LDs in non-adipose cell types.

Mitochondria-lipid droplet association promotes triglyceride synthesis

We reasoned that mitochondrial recruitment to LDs can expand LDs by enhancing the synthesis of triglycerides (TAGs). To test this, we assessed the effect of Plin5 overexpression on TAG synthesis. As before, we performed parallel experiments in cells expressing truncated Plin5Δ399-463 that lacks mitochondrial recruiting sequence but preserve lipolysis regulatory function (Figure 4F). Cells were incubated with BODIPY C12 558/568 (C12), a fluorophore-conjugated fatty acid, and thin layer chromatography (TLC) was used to resolve cellular lipid species (Rambold et al., 2015). Plin5 increased C12 incorporation into TAG by 52.1±14.3% while Plin5Δ399-463 increased C12 incorporation by only 11.0±2.5% relative to untransduced controls (Figures 6A–B). To confirm C12 incorporation was dependent on TAG synthesis, we incubated cells with Triacsin C, a potent inhibitor of fatty acid esterification into TAG (Figures 6C–D). Triacsin C decreased C12 incorporation into TAG by 43.5% and increased free C12 by 28.6%, confirming that C12 incorporation into TAG depends on esterification.

We reasoned that LD recruitment could promote TAG synthesis by fulfilling the energy requirements of ATP-dependent TAG synthesis reactions (Mashek et al., 2007; Prentki and Madiraju, 2012). To test this, we assessed the effect of the mitochondrial ATP Synthase inhibitor Oligomycin A on Plin5-enhanced TAG synthesis. C12 incorporation in Plin5

expressing cells was 17.8±3.6% more sensitive to Oligomycin inhibition compared to Plin5Δ399-463 and untransduced controls (Figures 6E–F). These results suggest that mitochondrial association to LDs enhance TAG synthesis in a mitochondrial ATP-dependent manner.

Peridroplet mitochondria have unique structure, fusion dynamics, and movement

Mitochondria are highly dynamic organelles that continuously undergo cycles of fusion and fission to regulate network morphology and distribute network content (Chen et al., 2005; Liesa and Shirihai, 2013; Nakada et al., 2001). We therefore hypothesized that PDM maintain unique functional and proteomic identity through distinct fusion-fission dynamics. To test this, we first assessed the morphology of PDM and CM in electron micrographs of mice adapted to thermoneutrality, where PDM are the most abundant. Mitochondria with direct contact to LDs had 93.2±22.9% larger cross-sectional area and 47.4±7.3% longer aspect ratio compared to mitochondria with no visible LD association (Figures 7A–C). Analysis of internal mitochondrial structure also revealed that cristae in mitochondria associated with LDs were arranged in perpendicular orientation to the axis of mitochondria-LD interface and were 12.0±0.9% shorter and 5.4±0.8% wider compared to mitochondria with no visible association to LDs (Figure S5A–C). To determine whether PDM structural specializations are preserved in cultured cells, we performed confocal microscopy in living brown adipocytes transduced with mitochondrially-targeted photo-activatable GFP (mtPAGFP). Transduced brown adipocytes were stained with TMRE to visualize the entire mitochondrial network. Individual mitochondria were photo-converted by 2-photon laser pulse and imaged immediately thereafter (Figure 6D). Quantitative image analysis confirmed that PDM are more elongated than CM in cultured cells (Figure 6E). These results suggest that PDM functional specialization is matched by specialized structure.

We next assessed the fusion activity of CM and PDM in cultured brown adipocytes using mtPAGFP. The dilution of mtPAGFP fluorescence intensity over time reflects fusion of photo-activated mitochondria with non-photo-activated mitochondria. A 150 μm^2 region of the cell containing primarily PDM or CM was photo-converted by 2-photon laser pulse and imaged continuously at 15-minute intervals. mtPAGFP dilution rate was significantly slower in PDM compared to CM (Figures 7F–G), suggesting that PDM have reduced fusion compared to CM and decreased content exchange with the rest of the mitochondrial network.

We reasoned that reduced PDM fusion could result from a reduction in one or more of the determinants of fusion: 1) Mitofusin (Mfn) expression, 2) mitochondrial membrane potential (MMP), and 3) mitochondrial motility (Twig et al., 2010). Western blot analysis ruled out Mfn expression as the cause of reduced fusion as Mfn2 expression was high in PDM relative to CM (Figure S5D–E). Additionally, MMP analysis using the membrane potential-sensitive dye TMRE showed that PDM do not have reduced MMP (Figures S5F–G). To determine whether LD association reduces fusion by decreasing mitochondrial motility, we next quantified mitochondrial displacement over time in time-lapse confocal imaging. PDM displacement rate was significantly lower compared to CM (Figures 7H–I), suggesting that LD anchoring reduces PDM fusion by arresting motility. Taken together, these results

suggest that PDM have reduced mitochondrial motility leading to decreased fusion activity that promotes their segregation from CM.

Peridroplet mitochondria have reduced Drp1 recruitment and OPA1 processing

The concomitant reduction in PDM fusion activity and marked elongation led us to hypothesize that reduced fusion rate is matched by reduced fission activity (Chen et al., 2003). To assess outer membrane fission, we measured the recruitment of Drp1 to mitochondria by immunofluorescence (Cereghetti et al., 2008). Drp1 was immunolabeled in cultured cells where the mitochondrial network was labelled by mitochondrially-targeted DsRed (mtDsRed). Confocal imaging revealed significantly lower Drp1 staining on PDM compared to CM (Figures 7J–K), suggesting lower outer membrane fission activity. Next, to assess inner membrane fission, we measured OPA1 processing in isolated mitochondria. Proteolytic cleavage of the long-forms OPA1 (L-OPA1) to short-OPA1 (S-OPA1) is associated with inner membrane fission (Anand et al., 2014). Western blot analysis revealed significantly lower levels of S-OPA1 in PDM compared to CM, suggesting lower inner membrane fission activity (Figures 7L–O). We reasoned that fission arrest can be a cause or a consequence of LD recruitment. To test this, we assessed mitochondrial LD association in cells expressing the dominant-negative Drp1 K38A (Drp1DN)(Smirnova et al., 2001). Drp1DN did not enhance mitochondrial recruitment to LDs (Figures 7P, S5H), suggesting that fission arrest is a consequence rather than a cause of LD recruitment. Taken together, these results suggest that LD association reduces fission protein recruitment and processing that promotes PDM elongation.

DISCUSSION

Peridroplet mitochondrial isolation by differential centrifugation

In this study we developed an approach to isolate intact respiring PDM and determine their bioenergetic function for the first time. Our approach took advantage of the buoyancy of LDs to separate LD-bound PDM from CM. PDM were then purified using high-speed centrifugation, a procedure previously shown to strip LD-associated proteins (Figure 1) (Ding et al., 2013; Yu et al., 2015). These results raise important considerations for the interpretation of past and future experiments with isolated mitochondria. First, mitochondrial isolation protocols that eliminate lipid fraction by aspiration (Rogers et al., 2011) and/or gauze filtration (Cannon and Nedergaard, 2001) may miss physiologically relevant changes that occur in PDM but not in CM. Second, isolation protocols that include an initial high-speed centrifugation step prior to low-speed centrifugation steps (Cannon and Nedergaard, 2001; Djafarzadeh and Jakob, 2017) may inadvertently strip LDs, resulting in a mixed population of CM and PDM. To our knowledge, this is the first report to specifically isolate intact respiring PDM from any tissue type and directly determine their functional role.

PDM have specialized oxidative phosphorylation protein composition and capacity

BAT mitochondria isolated by previous methods were shown to have low levels of ATP synthase elementary particles (Lindberg et al., 1967) and activity (Cannon and Vogel, 1977). Our study reveals that PDM have over two-fold higher ATP synthesis capacity matched by

enriched ATP synthase protein subunits when compared to CM, which may explain the relatively low levels of ATP synthesis reported in mitochondria isolated from BAT using previous methods. Consistent with higher ATP synthesis capacity, PDM were also enriched with cytochrome c oxidase and had increased electron transport capacity (Figure 3). We confirmed that higher respiration was not due to an artefactual difference in mitochondrial enrichment of PDM fraction by mass spectrometry analysis (Figure 1H) and imaging of mitochondria loaded within seahorse XF96 plates (Figures 2A–B). In addition, careful attention was dedicated to eliminate potential artifacts due to the presence of free fatty acids. Free fatty acids can alter respiration by 1) providing fuel for beta oxidation, 2) acting as weak uncouplers (Li et al., 2014), and 3) activating UCP1 (Fedorenko et al., 2012). To address this, we assessed the lipid contents of CM and PDM (Figures 1F–G) and supplemented the respiratory buffer with 0.1% BSA to remove free fatty acids from solution as well as 1mM of the UCP1 inhibitor GDP. ADP- and FCCP-stimulated respiration confirmed that mitochondria were coupled at the start of the assay. Free fatty acids could not serve as mitochondrial fuels in this system because the enzymes and cofactors required for acyl-CoA and acyl-carnitine syntheses are not present in assay buffer. Our results thus demonstrate that PDM represents a mitochondrial subpopulation with distinct bioenergetics and protein composition.

Peridroplet mitochondria are segregated by reduced fusion-fission dynamics

In every cell type where mitochondrial dynamics has been studied, mitochondria were shown to go through continuous cycles of fusion and fission that equilibrate the mitochondrial content across the mitochondrial population of the cell. We have previously reported that mitochondria in brown adipocytes continuously engage in fusion and fission activities (Wikstrom et al., 2014). The mechanism by which mitochondrial subpopulations can maintain separate function and composition in brown adipocytes was therefore unclear. Disparate mitochondrial subpopulations have been previously observed in tissues where mitochondrial subpopulations are separated in space (Wikstrom et al., 2009). For example, in striated muscle, it has been observed that subsarcolemmal mitochondria that are separated from interfibrillar mitochondria by the sarcomere have specialized form and function (Palmer et al., 1977). However, the brown adipocyte lacks the cytoplasmic subdivision that is mediated by myocyte sarcomeres and thus one expects fusion and fission to continuously equilibrate mitochondrial content across the adipocyte mitochondrial population (Wikstrom et al., 2014). Our results demonstrate that PDM have reduced fusion-fission dynamics that segregate them from the rest of the mitochondrial population (Figures 7F–G). Various evidence support that altered mitochondrial dynamics are a consequence rather than a cause of LD recruitment: 1) Neither fusion arrest (Boutant et al., 2017) nor fission arrest (Figures 8G–H) recruit mitochondria to LDs and 2) Mitochondrial recruitment to LDs by Plin5 promotes mitochondrial elongation (Wang et al., 2013). This supports the conclusion that reduced mitochondrial dynamics are a consequence rather than a cause of LD association. Furthermore, our observation that PDM are stationary (Figures 7H–I) suggests a mechanism by which LD association reduces mitochondrial dynamics, as we have previously shown that stationary mitochondria have markedly lower probability to undergo fusion (Twig et al., 2008, 2010). Our results thus suggest that PDM maintain functional and proteomic segregation from CM by having reduced motility and fusion-fission dynamics.

Peridroplet mitochondria are not associated with fatty acid oxidation

Recent studies have hypothesized that PDM facilitate fatty acid trafficking toward mitochondrial beta oxidation (Boutant et al., 2017; Rambold et al., 2015) while others have suggested that mitochondria-LD association enhances LD biogenesis and thereby protects mitochondria from lipotoxicity (Nguyen et al., 2017; Stone et al., 2009; Wang et al., 2011). In this study we employed brown adipose tissue, a system that robustly shifts from LD expansion under thermoneutral conditions to lipid oxidation under cold/adrenergic stimulus. If PDM facilitate fat oxidation, we reasoned mitochondria-LD association will increase during cold-induced thermogenesis, when fatty acid oxidation rate is maximal. However, contrary to the hypothesis, mitochondrial association with LDs was decreased by cold-exposure (Figures 4H–K). These results are consistent with the previously published observation that mitochondrial protein content is reduced in LDs isolated from BAT of cold-adapted mice compared to mice in thermoneutral environment (Yu et al., 2015, Table S6). Our analyses of isolated mitochondria confirmed that PDM have lower fatty acid oxidation capacity and higher TCA cycle capacity compared to CM (Figures 4A–G). Taken together, these results support the conclusion that PDM are not specialized for lipid oxidation in BAT.

Mitochondria-lipid droplet interaction enhances lipid droplet expansion

The high level of mitochondria-LD contact observed in BAT under thermoneutral conditions led us to hypothesize that PDM play a role in LD expansion. To test this, we induced mitochondrial recruitment to LDs using adenoviral-mediated Plin5 overexpression, which has been shown to recruit mitochondria to LDs in multiple cell and tissue types (Bosma et al., 2012; Wang et al., 2011, 2013). Importantly, we developed a system in which the specific effects of mitochondrial recruitment can be differentiated from other Plin5 effects, such as lipolytic regulation. Our results show that mitochondrial recruitment to LDs doubled the size of LDs (Figure 5). Furthermore, the capacity of PDM to promote the incorporation of free fatty acids into TAG was dependent on mitochondrial ATP synthesis (Figure 6). This observation supports the conclusion that PDM enhance LD expansion by providing ATP to the ATP-demanding process of acyl-CoA synthesis and lipid cycling (Prentki and Madiraju, 2012). In addition, the increased TCA cycle capacity we observed suggests that PDM may support LD expansion by providing citrate for de novo lipogenesis. Taken together, our results thus support the conclusion that PDM support LD expansion rather than oxidation.

We suggest that increased mitochondrial recruitment to LDs may be part of a generalized adaptive response in physiological conditions that require LD expansion, such as post-prandial lipid synthesis and storage. PDM-mediated LD expansion may also play a role in preventing muscle and liver injury from lipotoxicity in conditions of nutrient excess, such as obesity and hyperlipidemia. A better understanding of PDM and LD biology may therefore be important for developing new therapies for lipotoxic tissue injury and insulin resistance. Animal models in which mitochondria-LD association can be specifically modulated will be necessary to resolve such questions in future studies.

Limitations of study

This study is the first to isolate intact respiring PDM and determine their unique composition and bioenergetics. However, our study has several limitations. Limitations of

our PDM isolation approach include: 1. Mitochondrial isolation by differential centrifugation results in relatively crude preparations contaminated with other organelles and cellular compartments. Mass spectrometry analysis of CM and PDM preparations revealed that approximately half of the proteins present in CM and PDM preparations were mitochondrial (Figure 1H), in agreement with previously published reports (Forner et al., 2009). 2. Mitochondrial isolation by differential centrifugation pools all PDM into a single pellet. As such, inter-mitochondrial heterogeneity (Figures 3F–I) is lost in subsequent biochemical and functional assays, which may lead to under-estimation of differences between CM and PDM populations (Figures 3A–C). 3. PDM isolation by differential centrifugation may preferentially select for PDM attached to larger LDs with higher buoyancy. Small LDs with insufficient buoyancy could potentially contaminate the supernatant and CM pellet and lead to further under-estimation of the differences between isolated CM and PDM properties. 4. Our method used high-speed centrifugation to strip PDM from LDs, a procedure which may alter their function. However the close agreement between our proteomic and bioenergetic data in living cells and isolated mitochondria (Figures 2–3) suggests that isolated PDM preserved the metabolic phenotype observed in intact cells.

STAR METHODS

CONTACT FOR REAGENT AND RESOURCE SHARING

Requests for information on methods and reagents should be directed to Marc Liesa (mliesa@mednet.ucla.edu) or Orian Shirihai (oshirihai@mednet.ucla.edu).

EXPERIMENTAL MODELS AND SUBJECTS DETAILS

Mice—Mitochondria were isolated from 12-week-old male C57BL6/J mice and primary brown adipocytes were isolated from 3 to 4-week-old wild-type male C57BL6/J mice (Jackson lab, Bar Harbor, ME). Animals were fed standard chow (mouse diet 9F, PMI Nutrition International, Brentwood, MO) and maintained under controlled conditions (19–22°C and a 14:10 h light-dark cycle) until euthanasia by isofluorane. All animal procedures were performed in accordance with the Guide for Care and Use of Laboratory Animals of the NIH, and were approved by the Animal Subjects Committee of the University of California, Los Angeles, and the Boston University Institutional Guidelines for Animal Care.

Cell Culture

Primary brown adipocytes isolation and culture: Brown adipose cells were isolated and cultured as described in (Cannon and Nedergaard, 2001b). BAT was dissected from interscapular, subscapular, and cervical regions of three male mice, minced, and transferred to 10mL collagenase digestion buffer in 50mL Falcon tube (2mg/mL Collagenase Type II in 100 mM HEPES, 120 mM NaCl, 4.8 mM KCl, 1mM CaCl2, 4.5 mM Glucose, 1.5% BSA, pH 7.4). Collagenase digestion was performed in 37°C water incubator under constant agitation for 25 minutes with vortex agitation every 5 min. Digested tissue was homogenized with 18.5G needle and strained through 100 μm and 40 μm filters. 30mL of ice-cold DMEM was added to tissue digest and centrifuged at 200 × g for 10 minutes at 4°C in Sorvall ST

16R (Thermo) with TX-2 00 swinging bucket rotor. Media was carefully removed and the cell pellet re-suspended in 30mL ice-cold DMEM media. Cells were centrifuged again with the same settings. Next, the cell pellet was re-suspended 5mL growth medium (DMEM supplemented with 10% newborn calf serum (NCS), 4 mM Glutamine, 10 mM HEPES, 0.1mg/mL sodium ascorbate, 50 U/ml penicillin, 50 μg/mL streptomycin) and plated in 6-well plate (Corning). Cells were incubated in 37°C 8% CO2 incubator. 48 Hours are after isolation, the cells were washed to remove debris and media was replaced. 72 hours after isolation the cells were lifted using STEMPro Accutase, counted, and re-plated in differentiation media (growth media supplemented with 1 μM rosiglitazone maleate and 4 nM porcine insulin) in final experimental vessel. Cells were differentiated for 7 days and media was changed every other day. For transduction experiments, cells were transduced with virus in differentiation day 0–3.

Brown adipocyte immortalization: Brown preadipocytes immortalized by SV40T antigen were kindly provided by Drs. Pedro Quiros and Carlos Lopez-Otin (Quirós et al., 2012). Immortalized preadipocytes were differentiated for 7 days in culture medium supplemented with 20 nM insulin and 1 nM T3, 0.5 mM isobutylmethylxanthine, 0.5 μM dexamethasone, and 0.125 mM indomethacin (Fasshauer et al., 2000) in 37°C 5% CO2 incubator.

INS1 culture: INS-1 832/13 cells were cultured in RPMI 1640 medium supplemented with 10% fetal calf serum (FBS), 10 mM HEPES buffer, 1 mM pyruvate, 50 μM 2-β-mercaptoethanol, 50 U/ml penicillin and 50 μg/ml streptomycin. Cells were incubated in 37°C 5% CO2 incubator and used between passage 60 and 80.

METHODS DETAILS

Peridroplet Mitochondrial Isolation—All procedures were performed using pre-chilled equipment and solutions. Interscapular BAT from 6 mice was harvested and rinsed in PBS. Tissue was weighed, minced, and suspended in 6 mL (~1mL/100mg tissue) Sucrose-HEPES-EGTA buffer supplemented with BSA (SHE+BSA; 250 mM sucrose, 5 mM HEPES, 2 mM EGTA, 2% fatty acid-free BSA, pH 7.2). The preparation was then mechanically homogenized with 9 strokes in glass-teflon dounce homogenizer. The homogenate was then transferred to 50mL falcon tube (Corning) and centrifuged in Sorvall ST 16R (Thermo) with TX-200 swinging bucket rotor at 900 × g for 10 min at 4°C. Supernatant was carefully poured into a new ice-cold falcon tube so as to leave the fat layer in the original tube. Keeping the original tube horizontal, the fat layer was scraped into a second ice-cold falcon tube and re-suspended in SHE+BSA buffer. The two fractions were centrifuged again at 900 × g for 10 min at 4°C and then transferred into 2mL Eppendorf tubes and centrifuged in a microcentrifuge (Thermo) at 9,000 × g for 10 min at 4°C. The pellets were resuspended in SHE+BSA and centrifuged with the same settings once more. The pellets were then re-suspended in SHE without BSA and protein concentration was determined by BCA (Thermo). BSA was omitted from the final isolation buffer to prevent interference with BCA assay.

Fluorescence Microscopy

Imaging apparatus: All imaging was performed on Zeiss LSM710 and LSM880. Super-resolution imaging was performed with 63× Apochromat oil-immersion lens and AiryScan super-resolution detector (Huff et al., 2015). Low-resolution images were captured with 10× air objective. Live cell imaging was performed with humidified 5% CO_2 chamber on a temperature controlled stage.

Fluorophore excitation/emission: All fluorophores were excited on separate tracks to avoid artifacts due to bleed-through emission. DAPI was excited with 405nm 30mW laser and its emission captured through 485nm short-pass filter. BODIPY 493/503, Alexa-Fluor 488, MitoTracker green, and PAGFP were excited with 488nm 25mW Argon-ion laser and their emission captured through 500–550nm band-pass filter. Alexa-Fluor 546, TMRE, and mtDsRed were excited with 543nm 1mW Helium-Neon laser or 561nm 20mW diode-pumped solid-state laser and their emission captured through a 580–650nm band-pass filter. MitoTracker deep red was excited using 633nm 5mW Helium-Neon laser and its emission captured through a 645nm long-pass filter. Fat layer and isolated mitochondria: 1μL of re-suspended preparation was combined with 1μL SHE buffer supplemented with 1μM MitoTracker deep red and 1μM BODIPY 493/503 on a 1.0mm glass slide (EMS 71867) and covered with #1.5 thickness coverglass (EMS 72222). Imaging was performed using 63× Apochromat oil-immersion lens.

Live cells: Cells were seeded, transduced, and differentiated in glass-bottom confocal plates (MatTek P35G-0.170-14-C). On the day of the experiment, DAPI was loaded at 1μg/mL, BODIPY 493/503 was loaded at 200 nM and TMRE was loaded at 15 nM for 90 min followed by wash-out before imaging. DAPI and BODIPY were washed out while TMRE was present during imaging.

Image analysis: All image analysis was performed in FIJI (ImageJ, NIH). Individual mitochondrial fluorescence intensity and area were measured in FIJI and imported into Microsoft Excel. Mitochondria smaller than 10 pixels in area were not included in final analyses. Mitochondria within 0.5 μm of lipid droplet edge were defined as PDM while mitochondria beyond 0.5 μm peridroplet region were defined as CM. Step-by-step instructions available upon request.

Image presentation: Image contrast and brightness were not altered in any quantitative image analysis protocols. Brightness and contrast were optimized to properly display representative images in figure panels. Display settings are equivalent in images directly compared to one another (Figures 1B–C, 1F, 1I, 2J, 5B, 5G, 7F).

Isolated Mitochondria Proteomics—100 micrograms of isolated mitochondria were re-suspended in 6M Urea 100 mM Tris, pH 8.5 and then reduced and alkylated by incubation in 5 mM TCEP-HCL for 20 min at room temperature, in the dark (Langousis et al., 2016). Lys-C was introduced to the protein suspension at an enzyme to substrate ratio of 1:100, and incubated for 4 hours at 37°C. Samples w ere subsequently diluted to 2M Urea by addition of 100 mM Tris, pH 8.5. A final concentration of 1 mM $CaCl_2$ was added to the solution,

and Trypsin introduced at an enzyme to substrate ratio of 1:50 overnight at 37°C. Proteolytic digestion was quenched by the addition of formic acid to a final concentration of 5%. Prior to mass spectrometric analysis, samples were desalted on Pierce C18 StageTips and eluted in 40% ACN before vacuum drying and resuspension in 5% formic acid. Desalted samples were separated on a 100μM internal diameter, revered phase fused silica column packed with 18cm of 1.9 μM C18 particles (Dr. Maisch, GmbH) with an integrated 5μM pulled electrospray emitter. Gradient delivery as performed on an Easy nLC-1000 UHPLC at 300 nl/min, and MS/MS spectra generated by Data Dependent Acquisition on a Thermo Q-Exactive mass spectrometer. Data analysis was carried out using the Integrated Proteomics pipeline 2 (Integrated Proteomics Applications, Inc., San Diego, CA). Specifically, MS/MS spectra were searched with the ProLuCID algorithm, and PSM confidence was estimated by DTASelect. Search was performed against the Uniprot Mouse proteome containing only reviewed proteins, downloaded on 08/29/2016. Peptide spectrum identifications were filtered at a 1% maximum false detection rate as estimated by a target-decoy database search strategy. Protein identifications were only considered after reaching the requirement of a minimum of two confidently identified peptides. The IP2 pipeline provided normalized spectral abundance factor and spectral count calculations for set comparisons.

Isolated Mitochondria Respirometry—Isolated mitochondria were re-suspended in respiration buffer (100 mM KCl, 10 mM KH_2PO_4, 2 mM $MgCl_2$, 5 mM HEPES, 1 mM EGTA, 0.1% BSA, 1 mM GDP, pH 7.2) containing substrates (Mahdaviani et al., 2017). Four micrograms per well were loaded into Seahorse XF96 microplate in 20μL volume. The loaded plate was centrifuged at 2,000 × g for 5 min at 4°C and an ad ditional 115 μL of buffer+substrate was added to each well. Substrate concentrations were as follow: 5 mM Pyruvate + 5 mM Malate, 5mM Succinate + 2 μM Rotenone, 40 μM palmitoyl-Carnitine + 1 mM Malate. ADP was injected at port A (3.5 mM final concentration), 20 Oligomycin at port B (3.5 μM), FCCP at port C (4 μM) and Antimycin A at port D (4 μM). Mix and measure times were 0.5 minutes and 4 minutes, respectively. A 2 minute wait time was included for oligomycin-resistant respiration measurements.

Cytochrome C Oxidase Assay—Two micrograms of isolated mitochondria were re-suspended in respiration buffer and plated on a seahorse XF96 microplate. To control for respiration mediated by TCA and other electron transport complexes, we injected antimycin/rotenone injection at the start of the assay (Divakaruni et al., 2014). We confirmed that cytochrome c was not a limiting factor as supplementing assay media with exogenous cytochrome c did not alter TMPD/ascorbate-mediated respiration. We injected the COX-specific inhibitor sodium azide at the end of the assay to confirm that TMPD/ascorbate-driven respiration was specific to COX activity. As an additional control, we permeabilized mitochondria by freeze-thawing or using the permeabilization reagent alamethicin. We found no significant differences between freshly isolated and permeabilized mitochondria, confirming that TCA cycle did not contribute to TMPD/Ascorbate-driven respiration. Final compound concentrations were as follows: rotenone (2 μM), antimycin (2 μM), TMPD (100 μM), Ascorbate (10 mM), sodium azide (20 mM).

ATP Synthesis Assay—One microgram of isolated mitochondria were re-suspended in mitochondrial respiration buffer containing 5 mM pyruvate + 5 mM malate + 3.5 mM ADP and kept on ice (Wibom et al., 1990). 50 μL of this mixture was combined with 50 μL of Luciferin-luciferase mix in clear-bottom black 96-well plate (Corning) and measured immediately. We determined the optimal concentration of reagents and measurement settings on our instrument using HPLC-purified ATP standards. Luminescent counts were integrated over 0.5 seconds at 10 second intervals separated by 0.5 second orbital shaking on Spark M10 microplate reader (Tecan). To control for ATP synthesis by adenylate kinase, we assessed luminescence in parallel samples that were treated with the ATP synthase inhibitor oligomycin A. We confirmed ATP contamination of ADP preparation was minimal by assaying ADP by itself. The linear rate of luminescence increase was calculated to determine ATP synthesis rate.

Protein Gel Electrophoresis and Immunoblotting

SDS-PAGE: 10–20 μg of isolated mitochondrial protein was re-suspended in NuPAGE LDS Sample Buffer with protease inhibitor cocktail and incubated at 45C for 10 min. Samples were then loaded into 4–12% Bis-Tris precast gels (ThermoFisher Sci. NP0321) and electrophoresed in xCell SureLock (Novex) in constant voltage at 60V for 15 minutes (to clear stacking) and 150V for 45 minutes.

Blue native gel electrophoresis: 10–50 μg of isolated mitochondrial protein was re-suspended in 20 μL solubilization buffer (50mM Imidazole, 500mM 6-aminohexanoic acid, EDTA 1mM pH 7.0)(Wittig et al., 2006). 8 mg digitonin/mg of mitochondrial protein was added and samples were incubated on ice for 5 minutes. Since commercial digitonin is only 50% pure, we used 16 mg of crude powder to achieve 8mg (no re-crystallization). Digitonin was dissolved in PBS by boiling and stored at 4°C until use. Solubilized samples were centri fuged at maximal speed in a microcentrifuge (Thermo) for 30 min at 4°C. Pellet was discarded and supernatant wa s combined with 1 μL of 2.5% Coomassie G-250. Samples were loaded into NativePAGE 3–12% Bis-Tris gel and electrophoresed at 4°C in xCell SureLock (Novex) in constant voltage at 20V for 60 minutes and 200V for 120 minutes or until dye front exited the gel.

Immunoblotting: Proteins were transferred to methanol-activated PVDF membrane in xCell SureLock in 30V constant voltage for 1 hour at 4°C. Commassie was completely washed off blue native blots using 100% methanol. Blots were blocked with 5g/100mL non-fat dry milk in 0.5ml/L PBST (1mL/L Tween-20/PBS) and incubated with primary antibody diluted in 1g/100mL BSA/PBST overnight at 4°C. The next day, blots were washed 3×10min in PBST, probed with HRP-linked secondary antibodies diluted in blocking solution for 1 hour at room temperature, and rinsed again 3×10min in PBST. Detection was achieved by ECL-Plus reagent and imaging was performed with Typhoon 9410 Molecular Imager (Amersham). Image contrast was uniformly reduced to enhance visibility. Band densitometry was quantified using ImageJ Gel Plugin (NIH).

Immunofluorescence—Cells were cultured, transduced, and differentiated on coverslips and fixed at 4% vol/vol PFA for 15 min at room temperature. After washing in PBS, cells

were incubated in permeabilization buffer (2 μl/mL Triton X-100, 0.5 mg/mL Sodium Deoxycholate in PBS, pH 7.4) for 15 min at room temperature. Cells were then blocked with 3g/100mL BSA for 1 hour at room temperature. Next, cells were incubated with 1:200 primary antibody at 4°C overnight. The next day, cells were washed in P BS and incubated with 1:500 Anti-Mouse Alexa Fluor 488 or Anti-Mouse Alexa Fluor 546 secondary antibodies for 1 hour at room temperature. After washing in PBS, coverslips were mounted in MOWIOL on glass slide, air-dried, and stored at 4°C.

Citrate Synthase Assay—Citrate synthase activity was performed using 5,5′-Dithiobis(2-nitrobenzoic acid) (DTNB) (Spinazzi et al., 2012). Isolated mitochondria were re-suspended in 200mM Tris buffer containing 0.2% v/v Triton X-100 (pH 8.0), 100 μM DTNB, and 300 μM acetyl-CoA and loaded into a clear-bottom black 96-well plate. Baseline 412nm absorbance was measured using Spark M10 microplate reader (Tecan). Oxaloacetate was then added and 412nm absorbance was repeatedly measured at 20 second intervals. The linear rate of absorbance increase was calculated to determine citrate synthesis rate.

NADH Imaging—NADH autofluorescence was excited using 730nm 2-photon Chameleon Vision laser (Coherent) to give 365 nm photo-equivalence at the focal plane. 425–475nm emission was detected by ultra-high sensitivity Gallium Arsenide Phosphide detectors with non-descanned beampath to maximize emission collection and minimize laser power. To minimize artifacts due to phototoxicity and bleaching, image acquisition settings were optimized on a test cell that was not included in final image analysis. Images of analyzed cells were subsequently acquired using a single laser scan.

Electron Microscopy—Interscapular brown adipose tissue was harvested from mice acclimated to 28°C for 2–4 weeks and from mice acclimated to 6°C for 1–5 days. Small tissue fragme nts were fixed in 2% glutaraldehyde/2% paraformaldehyde in 0.1M phosphate buffer, pH 7.4, for 4 hours at room temperature (Cinti et al., 2002). Samples were post-fixed in 1% osmium tetroxide, dehydrated in ethanol, and embedded in epoxy resin. Thin sections were obtained by MTX ultramicrotome (RMC, Tucson, AZ), stained with lead citrate, and imaged with Philips CM10 transmission electron microscope (Philipis, Eindhoven, Netherlands). Imaging of cross-ruled grating of known distance was used to calibrate images.

Image analysis: Mitochondria were manually traced in electron micrographs and quantified in ImageJ. Aspect ratio was calculated as the major axis divided by the minor axis.

Virus Preparation—Plin5 and Plin5Δ399-463 constructs were a generous gift from Carole Sztalyrd (Wang et al., 2011). Plasmids were modified to express mKATE2 far-red fluorophore to enhance compatibility with fluorescent dyes and packaged into adenoviral particles (Welgen, Inc.). Viral infection was confirmed by mKATE2 fluorescence. Lentiviral particles for mtPAGFP, mtDsRed, and Drp1DN were generated as previously described in detail (Wikstrom et al., 2014).

Gene delivery: Pre-adipocytes and INS1 cells were incubated with 0.3 μL/mL of adenoviral preparation for 5 hours in complete culture media. This was sufficient to achieve infection in the majority of cells with little to no toxicity as assessed by cell division and viability. Fluorescent label and protein expression were detectable at differentiation day 7. Lentiviruses were delivered as previously described in detail (Wikstrom et al., 2014).

Lipolysis Assay—Cells were seeded, transduced and differentiated in 96-well plate. On the day of experiment, the cells were washed once and incubated with 100 μL Krebs-Ringer Bicarbonate Buffer (KRB; 119mM NaCl, 4.6mM KCl, 5mM NaHCO3, 2mM CaCl2, 1mM MgSO4, 0.15mM Na2HOP4, 0.4mM KH2PO4, 20mM HEPES, 5mM Glucose, pH 7.4) for 2 hours. KRB was collected and assayed for glycerol using Free Glycerol Colorimetric/ Fluorometric Assay Kit (BioVision) according to the manufacturer instructions.

Thin Layer Chromatography—Cells were seeded, transduced, and differentiated in 6-well plate. Cells were washed and incubated with overnight with 1 μM BODIPY C12 558/568 as previously described (Rambold et al., 2015). Cells were harvested using Accutase and spun down. Cellular lipids were extracted in chloroform and developed on aluminum-backed silica plates (Sigma 55811) using 1:2 cyclohexane:ethyl acetate. Plates were imaged using Typhoon 9410 Molecular Imager (Amersham) and spots were quantified using ImageJ Gel Plugin.

Mitochondrial Fusion Assay—Brown adipocytes were seeded, transduced, and differentiated in glass-bottom confocal plates (MatTek). mtPAGFP was activated using 750nm 2-photon Chameleon Vision laser (Coherent) to give 375nm photo-equivalence at the focal plane (Twig et al., 2008, 2010). The diffusion of mtPAGFP was assessed by repeatedly scanning the cell at 15 minute intervals. GFP fluorescence was quantified within the region of interest at every time point to assess diffusion. Diffusion of cytosolic mitochondria PAGFP reached as steady state within 40–50 minutes after photo-activation. At this time point, mitochondria that retained non-diluted GFP were defined as non-fusing mitochondria.

QUANTIFICATION AND STATISTICAL ANALYSIS

All data analyses were performed using GraphPad Prism 5 and Microsoft Excel. Raw data from each individual experiment was evaluated using an unpaired two-tailed t-test with 95% confidence in Prism. For data sets that did not pass the D'Agostino and Pearson omnibus normality test (alpha = 0.05), differences were evaluated using a two-tailed unpaired non-parametric Mann-Whitney test with 95% confidence. For repeated independent experiments, the raw data of CM and PDM from each individual experiment were normalized to the average value of all mitochondria in that specific experiment as shown in the formula below. Experiment-normalized data was then evaluated by a paired two-tailed t-test with 95% confidence.

$$CM_{normalized} = \frac{\sum CM_{raw\ values}/\text{number of CM replicates}}{\left(\sum CM_{raw\ values} + \sum PDM_{raw\ values}\right)/\text{total number of CM and PDM replicates}}$$

$$\mathrm{PDM}_{\mathrm{normalized}} = \frac{\sum \mathrm{PDM}_{\mathrm{raw\ values}}/\text{number of PDM replicates}}{\left(\sum \mathrm{CM}_{\mathrm{raw\ values}} + \sum \mathrm{PDM}_{\mathrm{raw\ values}}\right)/\text{total number of CM and PDM replicates}}$$

Supplementary Material

Refer to Web version on PubMed Central for supplementary material.

Acknowledgments

We would like to thank Carole Sztalyrd for guiding our lab into the field of PDM biology. We would like to thank Gilad Twig, Nathanael Miller, Kyle Trudeau, David Chess, and Michael Kirber for assistance with image acquisition and analysis. We would like to thank Anish Nag, Sarah Cohen, and Jennifer Lippincott-Schwartz for assistance with TLC and Aviva Joseph and Keith Luo for assistance with adenoviral generation. We would like to thank Pedro M. Quirós and Carlos López-Otín for assistance with brown adipocyte cell culture. We would like to thank Drs. Linsey Stiles, Dani Dagan, Evan Taddeo, Karel Erion, Ajit S. Divakaruni, Harold S. Sacks, Guy Las, Dovi Shlomo, Eleni Ritou, Nour Alsabeeh, Alicia Kowaltowski, Karen Reue, Andrea Havasi, Matthew Jones, José A. Enríquez, Susan K. Fried, and Martin Picard for helpful discussions and advice. IYB was funded by T32-DK007201 Training Program in Metabolism, Endocrinology, and Obesity. OSS is funded by NIH-NIDDK 5-R01DK099618-02. ML is funded by UCLA Department of Medicine Chair commitment and UCSD/UCLA Diabetes Research Center (DRC) grant (NIH P30 DK063491). MFO was supported by the Conselho Nacional de Desenvolvimento Cientifico e Tecnológico (CNPq,http://www.cnpq.br/) grant # 229526/2013-6. Additional support was provided by RO1DK56690 (BEC and OSS), DK46220 (BNORC adipocyte and metabolic Core), NIH R01 DK075017 (CS), and DK072488 (CS).

References

Anand R, Wai T, Baker MJ, Kladt N, Schauss AC, Rugarli E, Langer T. The i-AAA protease YME1L and OMA1 cleave OPA1 to balance mitochondrial fusion and fission. J. Cell Biol. 2014; 204:919–929. [PubMed: 24616225]

Bosma M, Minnaard R, Sparks LM, Schaart G, Losen M, de Baets MH, Duimel H, Kersten S, Bickel PE, Schrauwen P, et al. The lipid droplet coat protein perilipin 5 also localizes to muscle mitochondria. Histochem. Cell Biol. 2012; 137:205–216. [PubMed: 22127648]

Boutant M, Kulkarni SS, Joffraud M, Ratajczak J, Valera-Alberni M, Combe R, Zorzano A, Cantó C. Mfn2 is critical for brown adipose tissue thermogenic function. EMBO J. 2017; 36:1543–1558. [PubMed: 28348166]

Calvo SE, Clauser KR, Mootha VK. MitoCarta2.0: an updated inventory of mammalian mitochondrial proteins. Nucleic Acids Res. 2016; 44:D1251–1257. [PubMed: 26450961]

Cannon B, Nedergaard J. Respiratory and thermogenic capacities of cells and mitochondria from brown and white adipose tissue. Methods Mol. Biol. Clifton NJ. 2001; 155:295–303.

Cannon B, Nedergaard J. Brown adipose tissue: function and physiological significance. Physiol. Rev. 2004; 84:277–359. [PubMed: 14715917]

Cannon B, Vogel G. The mitochondrial ATPase of brown adipose tissue. Purification and comparison with the mitochondrial ATPase from beef heart. FEBS Lett. 1977; 76:284–289. [PubMed: 140818]

Cereghetti GM, Stangherlin A, de Brito OM, Chang CR, Blackstone C, Bernardi P, Scorrano L. Dephosphorylation by calcineurin regulates translocation of Drp1 to mitochondria. Proc. Natl. Acad. Sci. U. S. A. 2008; 105:15803–15808. [PubMed: 18838687]

Chen H, Detmer SA, Ewald AJ, Griffin EE, Fraser SE, Chan DC. Mitofusins Mfn1 and Mfn2 coordinately regulate mitochondrial fusion and are essential for embryonic development. J. Cell Biol. 2003; 160:189–200. [PubMed: 12527753]

Chen H, Chomyn A, Chan DC. Disruption of Fusion Results in Mitochondrial Heterogeneity and Dysfunction. J. Biol. Chem. 2005; 280:26185–26192. [PubMed: 15899901]

Cinti S, Cancello R, Zingaretti MC, Ceresi E, De Matteis R, Giordano A, Himms-Hagen J, Ricquier D. CL316,243 and cold stress induce heterogeneous expression of UCP1 mRNA and protein in rodent brown adipocytes. J. Histochem. Cytochem. Off. J. Histochem. Soc. 2002; 50:21–31.

Cottet-Rousselle C, Ronot X, Leverve X, Mayol J-F. Cytometric assessment of mitochondria using fluorescent probes. Cytom. Part J. Int. Soc. Anal. Cytol. 2011; 79:405–425.

Ding Y, Zhang S, Yang L, Na H, Zhang P, Zhang H, Wang Y, Chen Y, Yu J, Huo C, et al. Isolating lipid droplets from multiple species. Nat. Protoc. 2013; 8:43–51. [PubMed: 23222457]

Divakaruni AS, Rogers GW, Murphy AN. Measuring Mitochondrial Function in Permeabilized Cells Using the Seahorse XF Analyzer or a Clark-Type Oxygen Electrode. Curr. Protoc. Toxicol. 2014; 60 25.2.1-16.

Djafarzadeh S, Jakob SM. Isolation of Intact Mitochondria from Skeletal Muscle by Differential Centrifugation for High-resolution Respirometry Measurements. J. Vis. Exp. JoVE. 2017

Fasshauer M, Klein J, Ueki K, Kriauciunas KM, Benito M, White MF, Kahn CR. Essential role of insulin receptor substrate-2 in insulin stimulation of Glut4 translocation and glucose uptake in brown adipocytes. J. Biol. Chem. 2000; 275:25494–25501. [PubMed: 10829031]

Fedorenko A, Lishko PV, Kirichok Y. Mechanism of fatty-acid-dependent UCP1 uncoupling in brown fat mitochondria. Cell. 2012; 151:400–413. [PubMed: 23063128]

Forner F, Kumar C, Luber CA, Fromme T, Klingenspor M, Mann M. Proteome differences between brown and white fat mitochondria reveal specialized metabolic functions. Cell Metab. 2009; 10:324–335. [PubMed: 19808025]

Garland PB, Shepherd D, Nicholls DG, Ontko J. Energy-dependent control of the tricarboxylic acid cycle by fatty acid oxidation in rat liver mitochondria. Adv. Enzyme Regul. 1968; 6:3–30. [PubMed: 5720339]

Huff J, Bathe W, Netz R, Anhut T, Weisshart K. The Airyscan Detector from ZEISS Confocal Imaging with Improved Signal-to-Noise Ratio and Superresolution. 2015

Langousis G, Shimogawa MM, Saada EA, Vashisht AA, Spreafico R, Nager AR, Barshop WD, Nachury MV, Wohlschlegel JA, Hill KL. Loss of the BBSome perturbs endocytic trafficking and disrupts virulence of Trypanosoma brucei. Proc. Natl. Acad. Sci. 2016; 113:632–637. [PubMed: 26721397]

Lapuente-Brun E, Moreno-Loshuertos R, Acín-Pérez R, Latorre-Pellicer A, Colás C, Balsa E, Perales-Clemente E, Quirós PM, Calvo E, Rodríguez-Hernández MA, et al. Supercomplex assembly determines electron flux in the mitochondrial electron transport chain. Science. 2013; 340:1567–1570. [PubMed: 23812712]

Li Y, Fromme T, Schweizer S, Schöttl T, Klingenspor M. Taking control over intracellular fatty acid levels is essential for the analysis of thermogenic function in cultured primary brown and brite/beige adipocytes. EMBO Rep. 2014; 15:1069–1076. [PubMed: 25135951]

Liesa M, Shirihai OS. Mitochondrial dynamics in the regulation of nutrient utilization and energy expenditure. Cell Metab. 2013; 17:491–506. [PubMed: 23562075]

Lindberg O, de Pierre J, Rylander E, Afzelius BA. Studies of the mitochondrial energy-transfer system of brown adipose tissue. J. Cell Biol. 1967; 34:293–310. [PubMed: 6033537]

Mahdaviani K, Benador IY, Su S, Gharakhanian RA, Stiles L, Trudeau KM, Cardamone M, Enríquez-Zarralanga V, Ritou E, Aprahamian T, et al. Mfn2 deletion in brown adipose tissue protects from insulin resistance and impairs thermogenesis. EMBO Rep. 2017

Mashek DG, Li LO, Coleman RA. Long-chain acyl-CoA synthetases and fatty acid channeling. Future Lipidol. 2007; 2:465–476. [PubMed: 20354580]

Nakada K, Inoue K, Ono T, Isobe K, Ogura A, Goto YI, Nonaka I, Hayashi JI. Inter-mitochondrial complementation: Mitochondria-specific system preventing mice from expression of disease phenotypes by mutant mtDNA. Nat. Med. 2001; 7:934–940. [PubMed: 11479626]

Nguyen TB, Louie SM, Daniele JR, Tran Q, Dillin A, Zoncu R, Nomura DK, Olzmann JA. DGAT1-Dependent Lipid Droplet Biogenesis Protects Mitochondrial Function during Starvation-Induced Autophagy. Dev. Cell. 2017; 42:9–21.e5. [PubMed: 28697336]

Palmer JW, Tandler B, Hoppel CL. Biochemical properties of subsarcolemmal and interfibrillar mitochondria isolated from rat cardiac muscle. J. Biol. Chem. 1977; 252:8731–8739. [PubMed: 925018]

Prentki M, Madiraju SRM. Glycerolipid/free fatty acid cycle and islet β-cell function in health, obesity and diabetes. Mol. Cell. Endocrinol. 2012; 353:88–100. [PubMed: 22108437]

Rambold AS, Cohen S, Lippincott-Schwartz J. Fatty acid trafficking in starved cells: regulation by lipid droplet lipolysis, autophagy, and mitochondrial fusion dynamics. Dev. Cell. 2015; 32:678–692. [PubMed: 25752962]

Rogers GW, Brand MD, Petrosyan S, Ashok D, Elorza AA, Ferrick DA, Murphy AN. High Throughput Microplate Respiratory Measurements Using Minimal Quantities Of Isolated Mitochondria. PLOS ONE. 2011; 6:e21746. [PubMed: 21799747]

Rosca MG, Vazquez EJ, Kerner J, Parland W, Chandler MP, Stanley W, Sabbah HN, Hoppel CL. Cardiac mitochondria in heart failure: decrease in respirasomes and oxidative phosphorylation. Cardiovasc. Res. 2008; 80:30–39. [PubMed: 18710878]

Smirnova E, Griparic L, Shurland DL, van der Bliek AM. Dynamin-related protein Drp1 is required for mitochondrial division in mammalian cells. Mol. Biol. Cell. 2001; 12:2245–2256. [PubMed: 11514614]

Spinazzi M, Casarin A, Pertegato V, Salviati L, Angelini C. Assessment of mitochondrial respiratory chain enzymatic activities on tissues and cultured cells. Nat. Protoc. 2012; 7:1235–1246. [PubMed: 22653162]

Stone SJ, Levin MC, Zhou P, Han J, Walther TC, Farese RV. The endoplasmic reticulum enzyme DGAT2 is found in mitochondria-associated membranes and has a mitochondrial targeting signal that promotes its association with mitochondria. J. Biol. Chem. 2009; 284:5352–5361. [PubMed: 19049983]

Tarnopolsky MA, Rennie CD, Robertshaw HA, Fedak-Tarnopolsky SN, Devries MC, Hamadeh MJ. Influence of endurance exercise training and sex on intramyocellular lipid and mitochondrial ultrastructure, substrate use, and mitochondrial enzyme activity. Am. J. Physiol. Regul. Integr. Comp. Physiol. 2007; 292:R1271–1278. [PubMed: 17095651]

Twig G, Elorza A, Molina AJA, Mohamed H, Wikstrom JD, Walzer G, Stiles L, Haigh SE, Katz S, Las G, et al. Fission and selective fusion govern mitochondrial segregation and elimination by autophagy. EMBO J. 2008; 27:433–446. [PubMed: 18200046]

Twig G, Liu X, Liesa M, Wikstrom JD, Molina AJA, Las G, Yaniv G, Hajnóczky G, Shirihai OS. Biophysical properties of mitochondrial fusion events in pancreatic β-cells and cardiac cells unravel potential control mechanisms of its selectivity. Am. J. Physiol. - Cell Physiol. 2010; 299:C477–C487. [PubMed: 20445168]

Wang H, Sreenivasan U, Sreenevasan U, Hu H, Saladino A, Polster BM, Lund LM, Gong D, Stanley WC, Sztalryd C. Perilipin 5, a lipid droplet-associated protein, provides physical and metabolic linkage to mitochondria. J. Lipid Res. 2011; 52:2159–2168. [PubMed: 21885430]

Wang H, Sreenivasan U, Gong D-W, O'Connell KA, Dabkowski ER, Hecker PA, Ionica N, Konig M, Mahurkar A, Sun Y, et al. Cardiomyocyte-specific perilipin 5 overexpression leads to myocardial steatosis and modest cardiac dysfunction1. J. Lipid Res. 2013; 54:953–965. [PubMed: 23345411]

Wibom R, Lundin A, Hultman E. A sensitive method for measuring ATP-formation in rat muscle mitochondria. Scand. J. Clin. Lab. Invest. 1990; 50:143–152. [PubMed: 2339278]

Wikstrom JD, Twig G, Shirihai OS. What can mitochondrial heterogeneity tell us about mitochondrial dynamics and autophagy? Int. J. Biochem. Cell Biol. 2009; 41:1914–1927. [PubMed: 19549572]

Wikstrom JD, Mahdaviani K, Liesa M, Sereda SB, Si Y, Las G, Twig G, Petrovic N, Zingaretti C, Graham A, et al. Hormone-induced mitochondrial fission is utilized by brown adipocytes as an amplification pathway for energy expenditure. EMBO J. 2014; 33:418–436. [PubMed: 24431221]

Wittig I, Braun H-P, Schägger H. Blue native PAGE. Nat. Protoc. 2006; 1:418–428. [PubMed: 17406264]

Yu J, Zhang S, Cui L, Wang W, Na H, Zhu X, Li L, Xu G, Yang F, Christian M, et al. Lipid droplet remodeling and interaction with mitochondria in mouse brown adipose tissue during cold treatment. Biochim. Biophys. Acta. 2015; 1853:918–928. [PubMed: 25655664]

Highlights

- Peridroplet mitochondria (PDM) have enhanced bioenergetic capacity
- Peridroplet mitochondria have low fatty acid oxidation capacity
- PDM support lipid droplet expansion by providing ATP for triglyceride synthesis
- Distinct fusion-fission dynamics separate PDM from cytoplasmic mitochondria

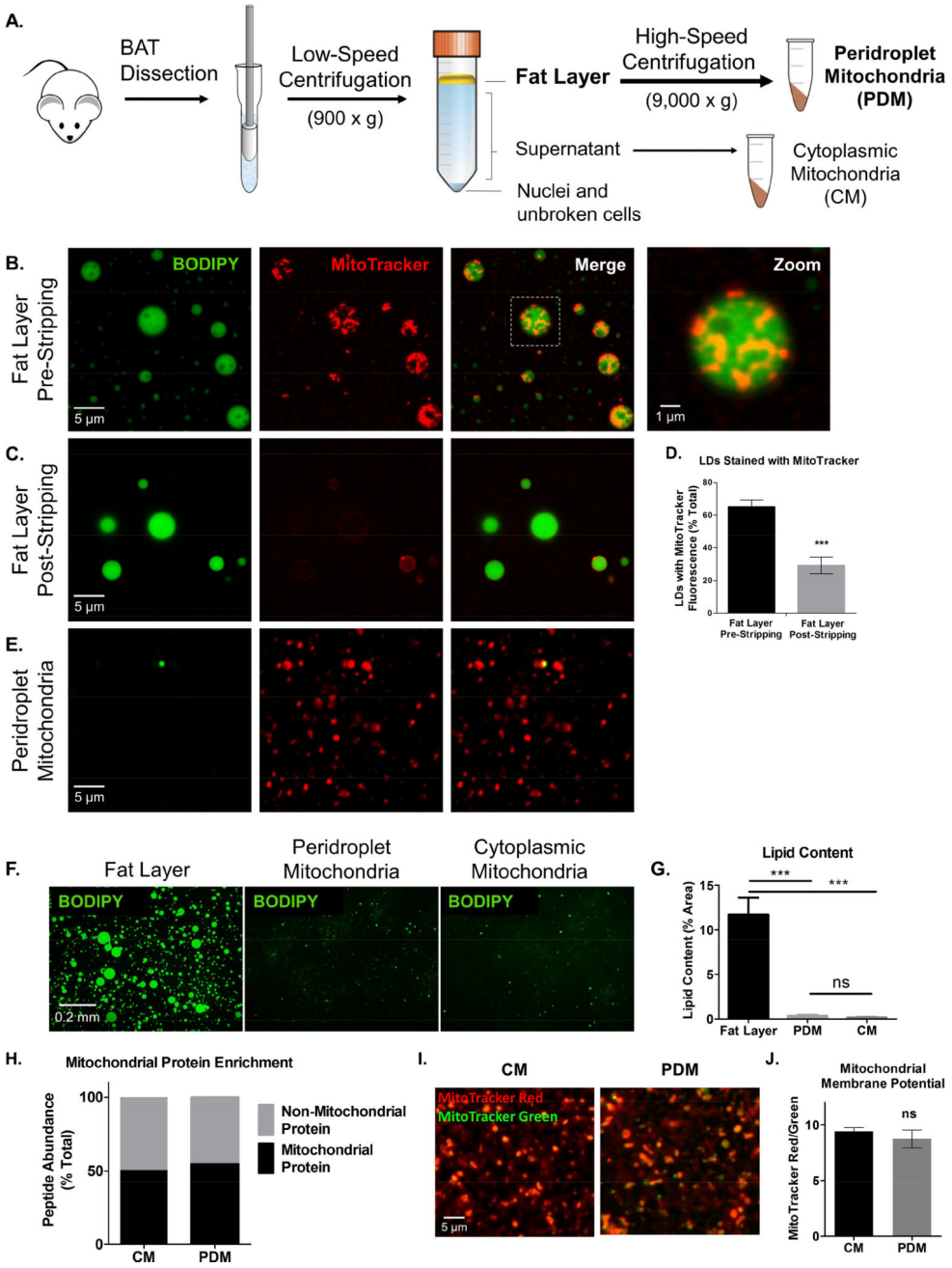

Figure 1. Isolation of peridroplet mitochondria by differential centrifugation

A. Schematic representation of peridroplet (PDM) and cytoplasmic (CM) mitochondrial isolation from interscapular brown adipose tissue (BAT). BAT was dissected from mice and homogenized with glass-Teflon dounce homogenizer. Low-speed centrifugation separated the fat layer containing PDM from supernatant containing CM. High-speed centrifugation stripped PDM from lipid droplets (LDs) and pelleted CM mitochondria from the supernatant. Note that some BAT mitochondrial isolation protocols discard the fat layer and/or begin with high-speed centrifugation step.

B–E. PDM are stripped from LDs by high-speed centrifugation.

B–C. Super-resolution confocal images of the fat layer before and after high-speed centrifugation. LDs were marked by the neutral BODIPY 493/503 fluorescent dye (BODIPY) and mitochondria by MitoTracker deep red dye (MitoTracker). Note the tubular structures staining positively for MitoTracker on LDs.

D. Quantification of LDs with MitoTracker staining in the fat layer pre- and post-stripping by high-speed centrifugation. 11,744 LDs were assessed in total. *** $p < 0.0001$.

E. Super-resolution confocal image of PDM pellet separated from fat layer by high-speed centrifugation.

F–G. Low-magnification (20×) images of the fat layer, PDM pellet, and CM pellet. LD content was assessed by BODIPY staining. 5–6 technical replicates per group. N = 3 independent isolations. ns $p>0.05$, *** $p < 0.0001$. One-way ANOVA with Tukey post-test.

H. Mass spectrometry analysis of relative mitochondrial protein content of CM and PDM preparations.

I–J. Analysis of CM and PDM membrane potential by fluorescence microscopy of CM and PDM double-stained with the membrane potential-sensitive dye MitoTracker Red and the mitochondrial protein dye MitoTracker Green. N = 15–22 images per group from 3 independent isolations. ns $p>0.05$.

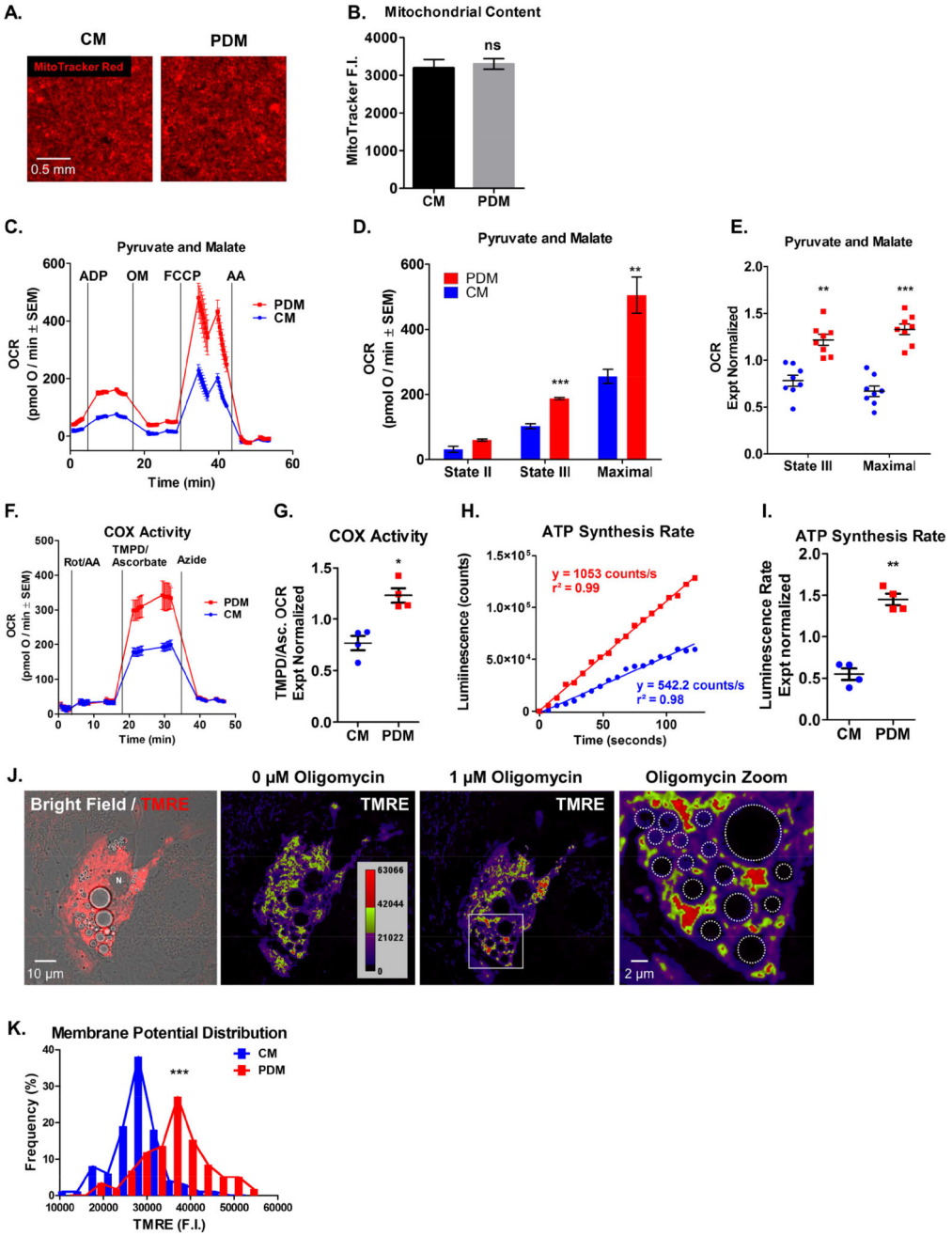

Figure 2. Peridroplet mitochondria have enhanced bioenergetic capacity

A–I. Peridroplet (PDM) and cytosolic (CM) mitochondria isolated from brown adipose tissue (BAT).

A. Fluorescence microscopy images of seahorse respirometry plate containing isolated CM and PDM stained with MitoTracker Red.

B. Quantification of MitoTracker Red fluorescence intensity (F.I.) in Seahorse wells loaded with CM or PDM. 5–7 wells quantified per condition.

C. Representative traces of oxygen consumption rates (OCRs) of isolated PDM and CM driven with pyruvate+malate. ADP, Oligomycin, FCCP, and Antimycin were sequentially injected to assess mitochondrial respiratory states. 4–6 technical replicates per group.
D. Quantification of OCR at different mitochondrial respiratory states in representative experiment. State II quantifies respiration driven proton leak (no ATP synthesis), State III quantifies respiration driven by ATP synthesis, and maximal respiration quantifies maximal electron transport activity induced by the chemical uncoupler FCCP. 6 technical replicates per group.
E. Quantification of mitochondrial respiratory states in N = 8 independent experiments. For each individual experiment, average OCR values of CM and PDM were normalized to the average OCR of all mitochondria (see Quantification and Statistical Analysis for complete equations).
F–G. Cytochrome C oxidase activity in PDM and CM isolated from BAT.
F. Representative traces of oxygen consumption rate (OCR) of isolated PDM and CM driven with the cytochrome c oxidase-specific substrates TMPD+Ascorbate. Rotenone and Antimycin were injected in the beginning of the assay to extinguish cytochrome c reduction by Complex I and Complex III. The COX-specific inhibitor sodium azide was injected at the end of the assay to control for non-COX respiration. 5 technical replicates per group.
G. Quantification of COX activity in N = 4 independent isolations. Data were normalized as in E. H–I. ATP synthase activity in PDM and CM isolated from BAT.
H. Representative traces of luciferase luminescence assay in isolated mitochondria normalized to baseline. ATP synthesis rates were determined by the rate of luminescence gain.
I. Quantification of ATP synthase activity in N = 4 independent isolations. Data were normalized as in E.
J–K. Confocal imaging of living cultured brown adipocytes stained with membrane potential-sensitive dye TMRE.
J. Confocal imaging before and after addition of the ATP synthase inhibitor Oligomycin. Bright field image was used to identify LDs. TMRE images were pseudo-colored for quantitative display (see calibration bar in top left). Note that PDM had higher fluorescence than CM after oligomycin treatment. White dashed circles denote LDs, white N denotes the nucleus, and white square denotes zoomed region.
K. Quantification of TMRE fluorescence intensity in oligomycin-treated brown adipocytes. 159 mitochondria were assessed in total. N = 33 cells collected in 6 independent experiments.
Data are expressed as means ± SEM. ns $p>0.05$, * $p< 0.05$, ** $p < 0.001$, *** $p < 0.0001$. See also Figure S1.

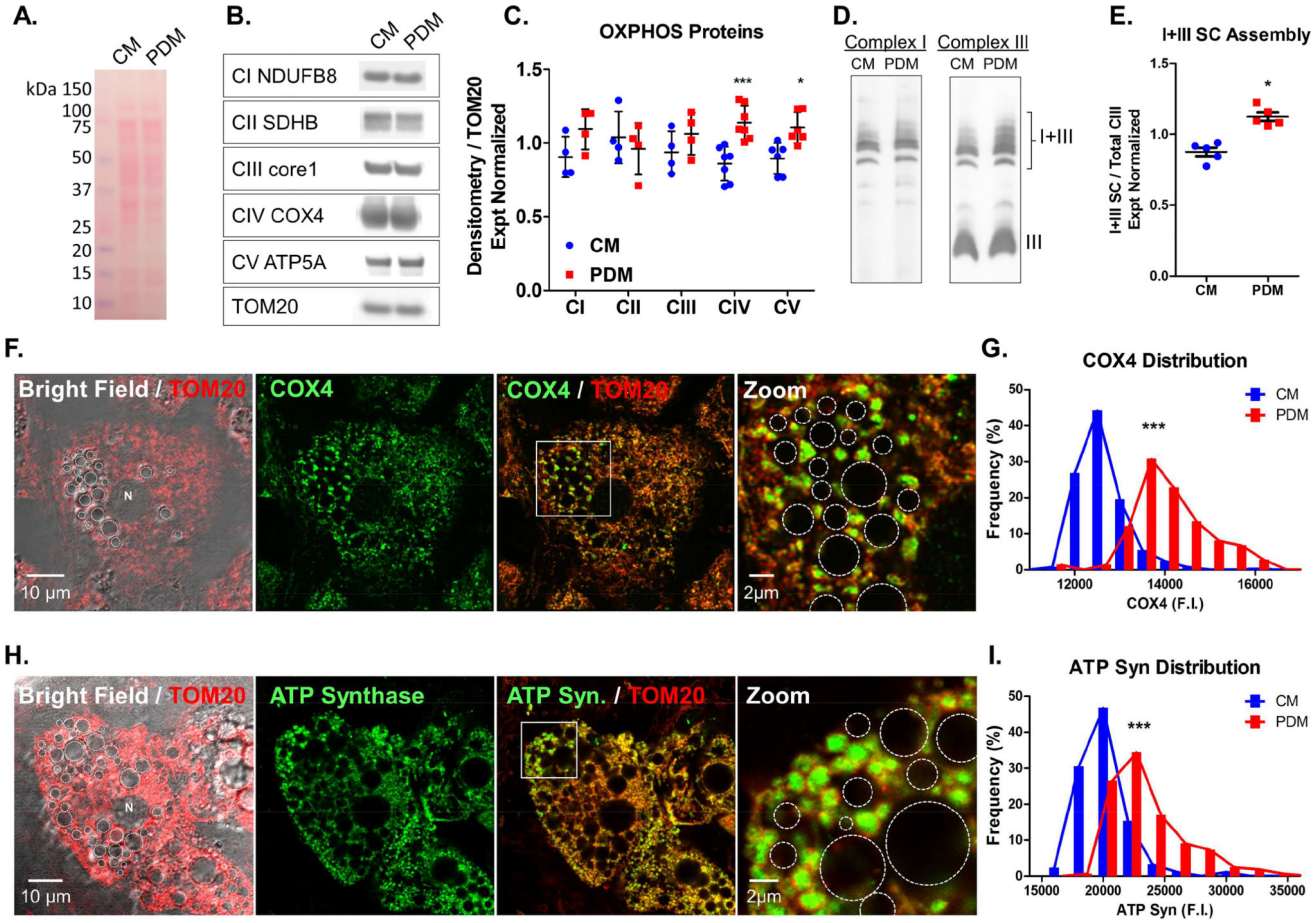

Figure 3. Peridroplet mitochondria have increased levels of cytochrome c oxidase, ATP synthase and super complex I+III assembly

A–C. Western blot analysis of Peridroplet (PDM) and cytosolic (CM) mitochondria isolated from brown adipose tissue (BAT).

A. Western blot of isolated CM and PDM stained with the dye Ponceau S for total protein loading.

B. Western blot probed with antibodies of OXPHOS complex subunits I–V (CI-CV) and Tom20 as a loading control.

C. Quantification of OXPHOS complex subunits normalized to Tom20 loading control in N = 4–7 independent isolations. For each individual experiment, average values of CM and PDM were normalized to the average OCR of all mitochondria (see Quantification and Statistical Analysis for complete equations).

D–E. Western blot of Blue Native PAGE of PDM and CM isolated from BAT.

D. Western blot of assembled Complex I and Complex III in isolated mitochondria.

E. Quantification of Complex III assembled into I+III supercomplexes relative to total Complex III. N = 5 independent isolations. Data were normalized as in C.

F–I. Super-resolution confocal imaging of fixed cultured brown adipocytes (no adrenergic stimulation).

F. Brown adipocytes immunostained for COX4. Bright field image was used to identify LDs and TOM20 immunostaining was used to mark the mitochondrial network. White dashed circles denote LDs, white N denotes the nucleus, and white square denotes zoomed region.
G. Quantification of COX4 distribution in brown adipocyte mitochondria. 490 mitochondria were assessed in total. N = 22 cells collected in 3 independent experiments.
H. Brown adipocytes immunostained for ATP Synthase. Bright field image was used to identify LDs and TOM20 immunostaining was used to mark the mitochondrial network. White dashed circles denote LDs, white N denotes the nucleus, and white square denotes zoomed region.
I. Quantification of ATP Synthase distribution in brown adipocyte mitochondria. 507 mitochondria were assessed in total. N = 20 cells collected in 4 independent experiments.
Data are expressed as means ± SEM. * $p< 0.05$, *** $p < 0.0001$.
See also Figure S2.

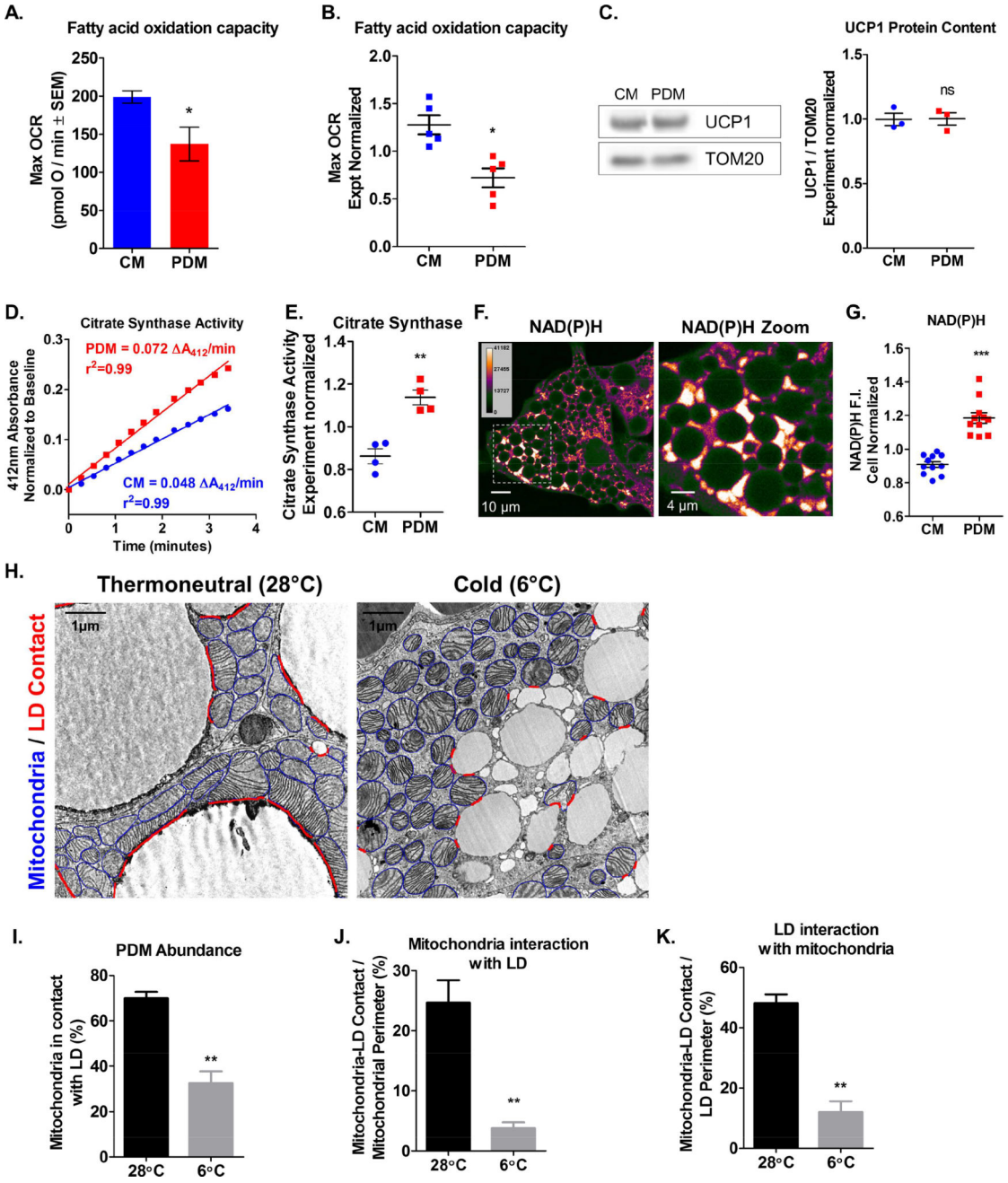

Figure 4. Peridroplet mitochondria have decreased fatty acid oxidation capacity and mitochondria-LD contact is decreased upon activation of thermogenic fatty acid oxidation *in vivo*

A. PDM have lower fatty acid oxidation capacity. Representative quantification of maximal palmitoyl-carnitine driven oxygen consumption rate (Max OCR) in isolated peridroplet (PDM) and cytoplasmic (CM) mitochondria. 4–6 technical replicates per group.

B. Quantification of palmitoyl-carnitine oxidation capacity. N = 5 independent experiments. For each individual experiment, average OCR values of CM and PDM were normalized to the average OCR of total mitochondria (see Quantification and Statistical Analysis for full equations).

C. UCP1 protein is similarly abundant in PDM and CM. Western blot analysis of UCP1 in CM and PDM. N = 3 independent mitochondrial isolations. Data were normalized as in B.
D–E. PDM have higher activity of the TCA cycle enzyme Citrate Synthase.
D. Representative traces of citrate synthase DTNB absorbance assay in isolated mitochondria normalized to baseline. Citrate synthase activity was determined for CM and PDM by the rate of absorbance gain.
E. Quantification of citrate synthase specific activity. N = 4 independent mitochondrial isolations. Data were normalized as in B.
F–G. PDM have increased NAD(P)H content.
F. Confocal image of NAD(P)H fluorescence in living cultured brown adipocytes. Image was pseudo-colored for quantitative display (see calibration bar in top left). Note the high level of NAD(P)H in PDM.
G. Quantification of NAD(P)H level. N = 24 cells imaged in 6 independent experiments. CM and PDM fluorescent intensities (F.I.) were normalized to average cell F.I. for each individual cell.
H. Electron micrographs (EMs) of BAT harvested from mice adapted to thermoneutral conditions (28°C), where fatty acids are stored in lipid droplets, and cold environment (6°C), where thermogenic fatty acid oxi dation is robustly increased. Blue lines highlight mitochondrial perimeter and red lines highlight overlap between mitochondria and LD border.
I–K. Mitochondria in contact with LD quantified by count, % mitochondrial perimeter and % LD perimeter. N = 10 EMs per condition.
Data are expressed as means ± SEM. ns $p>0.05$, * $p< 0.05$, ** $p < 0.001$, *** $p < 0.0001$.
See also Figure S3.

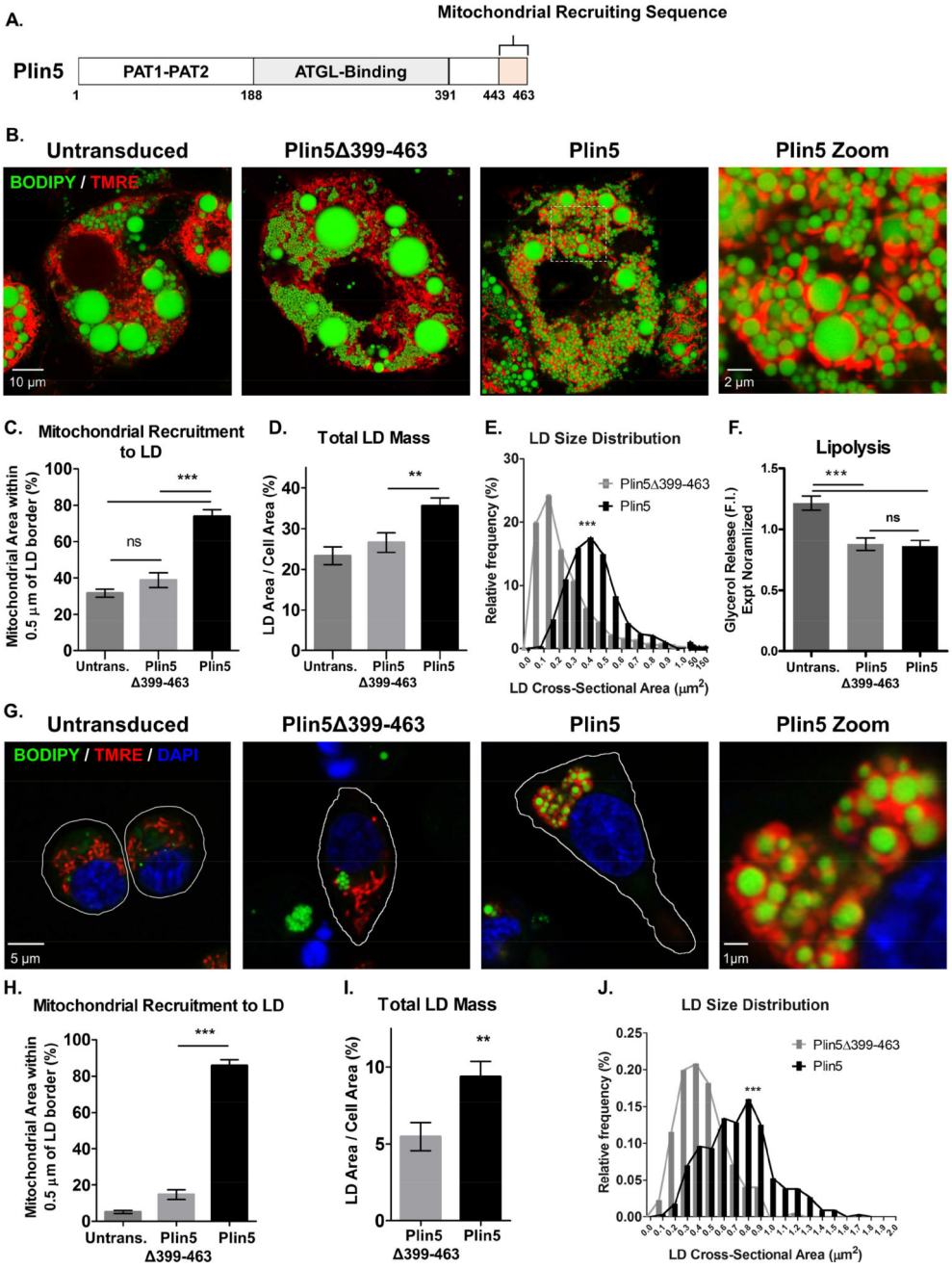

Figure 5. Mitochondria-lipid droplet association promotes lipid droplet expansion

A. Schematic representation of Perilipin5 (Plin5) domains: the conserved perilipin domains PAT1 and PAT2, the ATGL-binding domain responsible for lipolysis regulation, and the mitochondrial recruiting sequence.

B. Super-resolution confocal images of living brown adipocytes untransduced (control), transduced with the full-length Plin5 that contains mitochondrial recruiting sequence, and truncated Plin5 that lacks the mitochondria recruitment sequence (Plin5Δ399-463). Mitochondria are marked by TMRE staining and lipid droplets (LDs) by BODIPY 493/503. Note the increased lipid droplet (LD) mass and mitochondrial recruitment in Plin5.

C. Quantification of mitochondrial recruitment to LDs assessed as the area of mitochondria within 0.5 μm of LD border. N = 14–24 cells analyzed per group from 4 independent experiments.
D. Quantification of LD mass by cross-sectional area of BODIPY 493/503 normalized to cell area. N = 17–33 cells per group from 4 independent experiments.
E. LD size distribution assessed by cross-sectional area of individual LDs. N = 302–489 LDs per group from 4 independent experiments.
F. Quantification of lipolysis by glycerol release assay. N = 3 independent experiments. For each individual experiment, average values of CM and PDM were normalized to the average values of total mitochondria (see Quantification and Statistical Analysis for full equations).
G. Super-resolution confocal images of living INS1 pancreatic beta cell line untransduced (control), transduced with Plin5, and Plin5Δ399-463 and stained with TMRE to mark mitochondria and BODIPY 493/503 to mark LDs. Note the increased LD mass and mitochondrial recruitment in Plin5.
H. Quantification of mitochondrial recruitment to LDs assessed as the area of mitochondria within 0.5 μm of LD border. N = 12–20 cells analyzed per group from 3 independent experiments.
I. Quantification of LD mass by cross-sectional area of BODIPY 493/503 normalized to cell area. N = 13–19 cells per group from 3 independent experiments.
J. LD size distribution assessed by cross-sectional area of individual LDs. N = 226–344 LDs per group from 3 independent experiments.
Data are expressed as means ± SEM. ns $p>0.05$, * $p< 0.05$, ** $p < 0.001$, *** $p < 0.0001$. See also Figure S4.

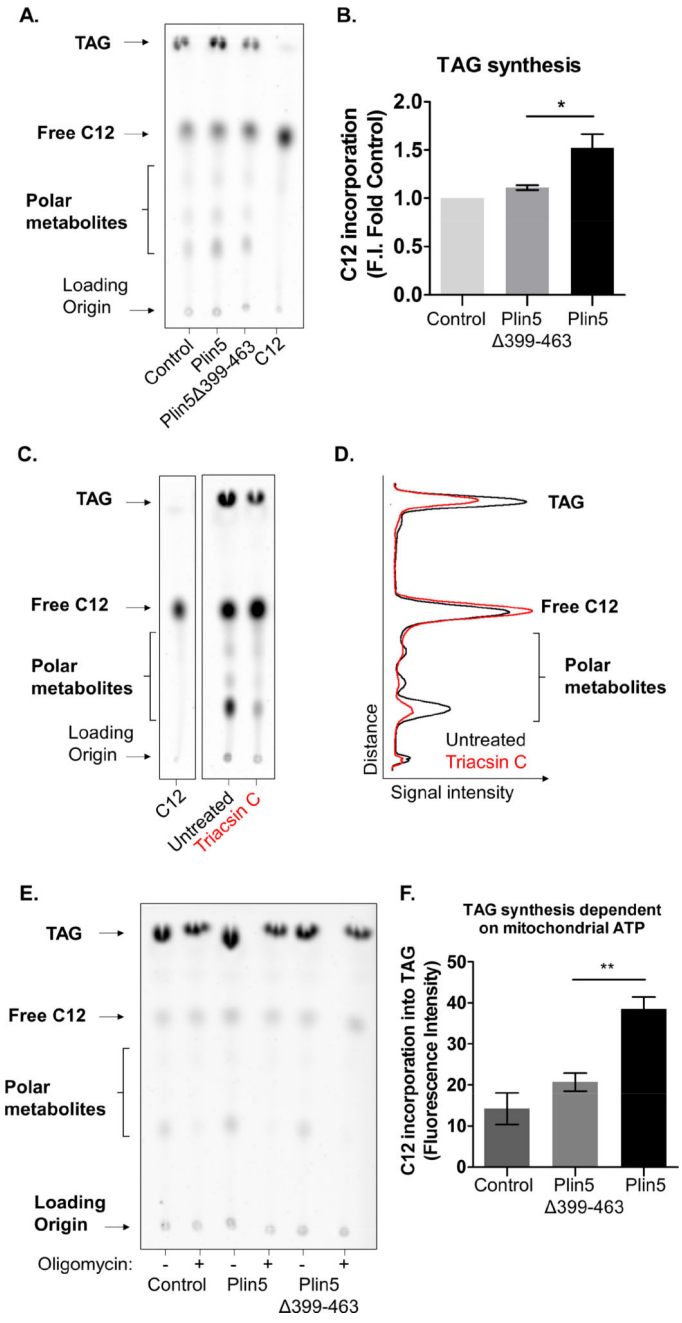

Figure 6. Mitochondria-lipid droplet association promotes triglyceride synthesis

A. Representative thin layer chromatography (TLC) of cellular lipids extracted from cultured brown adipocytes untransduced (control), transduced with the full-length Plin5 that contains mitochondrial recruiting sequence, and truncated Plin5 that lacks the mitochondria recruitment sequence (Plin5Δ399-463). Cells were incubated with BODIPY C12 558/568 (C12) overnight to assess triacylglyceride (TAG) synthesis. The mobility of fatty acids species from loading origin is determined by relative polarity, with TAG migrating the highest.

B. Quantification of TAG from N = 3 independent experiments. Data were normalized to control for each individual experiment.

C–D. TLC of cultured brown adipocytes incubated with C12 with or without the fatty acid esterification inhibitor Triacsin C (red). In histogram, note the decrease in TAG and increase in Free C12 induced by Triacsin C.

E. Representative TLC of cultured brown adipocytes incubated with C12 with or without the mitochondrial ATP synthase inhibitor Oligomycin.

F. Quantification of TAG synthesis dependent on mitochondrial ATP from N = 3 independent experiments. Mitochondrial ATP-dependent TAG synthesis was calculated as the difference in TAG between Oligomycin-treated and untreated cells.

Data are expressed as means ± SEM. * $p < 0.05$, ** $p < 0.001$.

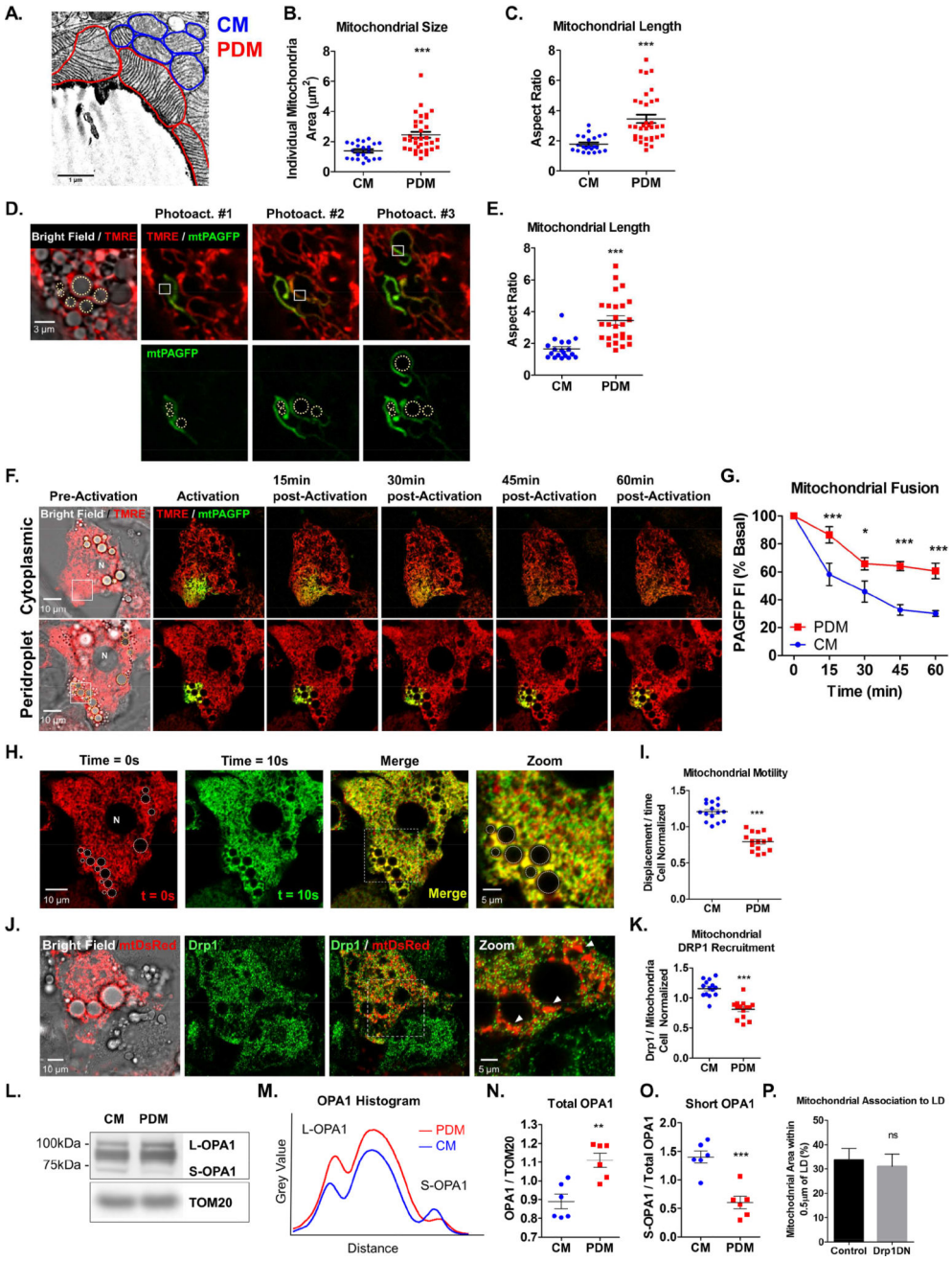

Figure 7. Peridroplet mitochondria have unique structure, fusion-fission dynamics, and motility

A–C. Electron micrograph (EMs) of BAT harvested from mice adapted to thermoneutral conditions (28°C), where peridroplet mitochondria (PDM) are most abundant. Red lines highlight PDM and blue lines highlight cytoplasmic mitochondria (CM). Note the elongation of PDM. Mitochondrial size and shape were quantified in N = 22 – 34 mitochondria from 10 EMs per group.

D–E. Confocal microscopy of living cultured brown adipocytes.

D. Confocal images of brown adipocytes transduced with mitochondrially-targeted photo-activatable GFP (mtPAGFP) stained with TMRE to label the mitochondrial network.

mtPAGFP in single mitochondria (white squares) were sequentially photo-converted and imaged immediately. Filled grey circles denote lipid droplets.

E. Quantification of mitochondrial shape, as delineated by mtPAGFP. N = 47 mitochondria from 4 independent imaging experiments.

F–G. Mitochondrial fusion assay in living cultured brown adipocytes. Brown adipocytes transduced mtPAGFP were stained with TMRE to label the mitochondrial network. White dashed circles denote LDs and white N denotes the nucleus. mtPAGFP was photo-converted in a small region of the cell (white squares) and its fluorescence intensity tracked over time. The dilution of mtPAGFP fluorescence intensity over time results from fusion between activated mitochondria with non-activated mitochondria. N = 5 cells per group imaged in 3 independent experiments. Data were normalized to baseline and statistically analyzed by Two-Way ANOVA for repeated measures with Bonferroni post-test.

H–I. PDM have reduced motility compared to CM.

H. Psudo-colored confocal images of brown adipocyte at two different time points (red and green). Merged image of two time points reveals immobile mitochondria (yellow) and mobile mitochondria that change position over time (red and green). White dashed circles denote LDs, white N denotes the nucleus, and white dashed square denotes zoomed region. Note the reduced mobility of PDM compared to CM.

I. Quantification of mitochondrial motility. Mitochondrial motility was quantified in time-lapse images as the percent of area displaced over a period of 10 seconds. For each individual cell, CM and PDM motility values were normalized to the average motility value of all mitochondria in the cell. N = 15 cells images in 3 independent experiments.

J. Confocal image of fixed cultured brown adipocytes immunolabeled for the mitochondrial fission protein Drp1. LDs were identified by bright field images and the mitochondrial network was marked with mitochondrially-targeted DsRed (mtDsRed). Note the low levels of Drp1 recruitment to PDM (white arrows).

K. Quantification of Drp1 associated with CM and PDM. Drp1 association was quantified as puncta area divided by mitochondrial area. In each individual cell, Drp1 association to CM and PDM values were normalized to the average of the entire cell. N = 14 cells per group imaged in 3 independent experiments.

L–O. Western blot analysis of the mitochondrial inner membrane protein OPA1 in isolated PDM and CM. Proteolytic cleavage of the long-forms OPA1 (L-OPA1) to short-OPA1 (S-OPA1) is associated with inner membrane fission. Densitometry of L-OPA1 and S-OPA1 in PDM and CM are shown in representative histogram.

N–O. Quantification of total OPA1 and S-OPA1 in CM and PDM. N = 6–7 independent mitochondrial isolations.

G. Confocal images of living primary brown adipocytes transduced with Drp1-dominant negative (Drp1DN) and transduction control. LDs were identified by bright field images and the mitochondrial network was marked with TMRE.

P. Fission arrest by Drp1 dominant negative (Drp1DN) expression does not recruit mitochondria to LD surface compared to transduction control. Mitochondrial recruitment was assessed as the area of mitochondria within 0.5 μm of LD border. N = 10 cells analyzed per group.

Data are expressed as means ± SEM. ns $p > 0.05$, * $p < 0.05$, ** $p < 0.001$, *** $p < 0.0001$.

See also Figure S5.